J. Fluid Mech. (2010), *vol.* 657, *pp.* 89–125. © Cambridge University Press 2010
doi:10.1017/S0022112010001382

Drag and lift forces on a spherical particle moving on a wall in a shear flow at finite *Re*

HYUNGOO LEE AND S. BALACHANDAR†

Department of Mechanical and Aerospace Engineering, University of Florida, Gainesville, FL 32611, USA

(Received 2 November 2009; revised 13 March 2010; accepted 13 March 2010; first published online 10 June 2010)

Recent research (Zeng, PhD thesis, 2007; Zeng *et al.*, *Phys. Fluids*, vol. 21, 2009, art. no. 033302) has shown that both the shear- and wall-induced lift contributions on a particle sharply increase as the gap between the wall and the particle is decreased. Explicit expressions that are valid over a range of finite *Re* were obtained for the drag and lift forces in the limiting cases of a stationary particle in wall-bounded linear flow and of a particle translating parallel to a wall in a quiescent ambient. Here we consider the more general case of a translating and rotating particle in a wall-bounded linear shear flow where shear, translational and rotational effects superpose. We have considered a modest Reynolds number range of 1–100. Direct numerical simulations using immersed boundary method were performed to systematically figure out the characteristics of hydrodynamic forces on a finite-sized particle moving while almost in contact with a wall. We present composite correlation for the hydrodynamic forces which are in agreement with all the available low-Reynolds-number theories.

1. Introduction

The hydrodynamic force on a finite-sized particle moving in a linear shear flow close to a wall is a problem of fundamental importance in fluid mechanics. The significance of this problem arises from its many practical industrial and environmental applications. Some examples are dust removal from surfaces, droplet deposition and resuspension of sand particles.

The effect of the wall is the strongest when the particle is in contact. The wall effect decays rapidly as the distance between the particle and wall increases. For distances of the order of 10 particle diameters or more, the wall effect can be reasonably ignored (Goldman, Cox & Brenner 1967*a*, *b*). For example, in the case of a stationary particle in contact with a flat wall, at low Reynolds numbers in a linear shear flow, the drag coefficient is 70 % larger than what would be predicted by Stokes drag for an unbounded uniform flow. Instead, if we consider a particle translating parallel to a flat wall in a stagnant fluid, in the limit of particle touching and sliding on the wall, there is a lubrication singularity. As the gap between the particle and the wall decreases, the drag force logarithmically increases and becomes infinite when the particle comes into contact with the wall. For instance, in the Stokes limit when the gap between the particle and the wall is 7 % of particle diameter, the drag force will be twice that when the wall is far away (Goldman *et al.* 1967*a*). This strong influence of the wall on the drag force has been shown to persist even at finite Reynolds numbers (Zeng *et al.* 2009).

---

† Email address for correspondence: bala1s@ufl.edu

The wall has a similar stronger influence on the lift force. There are three hydrodynamic contributions to the lift force on a particle. In a shear flow, the particle experiences the Saffman lift force (Saffman 1965). In a quiescent fluid, a particle travelling parallel to a wall will experience a wall-induced lift force that is directed normal to its motion (normal to the wall). Finally, a particle spinning either in a uniform cross-flow or close to a wall in a quiescent fluid will experience a rotation-induced lift force. The former is generally referred to as the Magnus lift and was considered by Rubinow & Keller (1961). All these lift forces are inertial in origin and are absent in a Stokes flow.

The problem of inertial lift on a stationary particle in contact with a flat wall in a linear shear flow was analytically considered by Leighton & Acrivos (1985). This analysis was later extended to the case of a translating and rotating particle in contact with the wall by Krishnan & Leighton (1995). It was shown that the lift force can be separated into six contributions. Three of the contributions arise from the ambient shear, and the translational and rotational motions of the particle. The other three contributions arise from shear–translation, translation–rotation and shear–rotation binary couplings. These low-Reynolds-number results were confirmed later by high-quality experiments (King & Leighton 1997).

The lift force is at its peak when the particle is in contact with the wall and falls off quite rapidly as the gap between the particle and the wall increases. There have been a number of asymptotic analyses that consider lift force on a particle in a shear flow located near a flat wall. But most of these analyses do not consider the limit of the particle touching the wall. The low-Reynolds-number asymptotic analysis of Cherukat & McLaughlin (1994) is relevant, as it considered lift force on a particle for arbitrary values of the gap between the particle and the wall. They presented results only for the cases of no rotation and torque-free rotation of the particle (also see Cherukat & McLaughlin 1994). In comparison, Krishnan & Leighton's (1995) analysis is valid for arbitrary translational and rotational motions of the particle, but when the particle is in contact with the wall. Nevertheless, Cherukat & McLaughlin's results in the zero-gap limit are in excellent agreement with those of Krishnan & Leighton. In particular, the results of Cherukat & McLaughlin for the case of a non-rotating particle can be recast as an additive superposition of shear, translation- and shear–translation contributions, suggesting the applicability of the superposition presented in Krishnan & Leighton (1995) even when the particle is away from the wall.

Hall (1988) and Mollinger *et al.* (1996) measured lift on a stationary spherical particle in contact with a wall in a turbulent boundary layer and observed the lift to be substantially larger than what would be predicted by Saffman lift in an unbounded shear of the same magnitude. Later, Muthanna *et al.* (2005) measured lift force on a stationary particle attached to a wall in a laminar linear shear layer and again the effect of the wall was to substantially increase the lift force. Since the particle was not allowed to move in these experiments, the implication is that wall–shear interaction results in substantial enhancement of the lift force over pure shear-induced lift in an unbounded shear flow.

For a particle not in contact with the wall, the non-dimensional gap between the wall and the bottom of the particle (non-dimensionalized by the particle diameter) is a key parameter. The analysis of Cherukat & McLaughlin (1994) is limited to the wall being in the inner (viscous) region on the particle. This places a strong restriction on the Reynolds number range over which the results are applicable. This restriction can be relaxed if we consider larger gap values. In the limit of large gap, the wall being in the inner region or in the outer region has been analytically considered (for example, see Cox & Hsu 1977; McLaughlin 1993; Magnaudet 2003).

The problem of drag and lift forces on a translating and rotating particle in a shear flow close to a wall is characterized by the non-dimensional gap and three Reynolds numbers – shear, translation and rotation Reynolds numbers. The results of Krishnan & Leighton provide a complete description of the lift force in the limit of zero gap and low Reynolds numbers. The other theoretical works mentioned above together provide substantial (but not complete) description of the lift force for arbitrary gap, provided all three Reynolds numbers are small.

The purpose of this paper is to consider the problem of a particle translating and rotating on a flat wall in a linear shear flow and obtain results in the finite-Reynolds-number regime and work towards a superposition of drag and lift contributions from shear, translation and rotation mechanisms that are applicable at modest Reynolds numbers. Fortunately, aspects of this complex problem have been considered in the past. The problem of a bubble (clean and contaminated) moving parallel to a flat wall in a quiescent fluid at finite *Re* was experimentally considered by Takemura *et al.* (2002) and Takemura & Magnaudet (2003). These results were computationally extended to rigid particles and higher Reynolds numbers by Zeng, Balachandar & Fischer (2005) and Zeng *et al.* (2008). The above experiments and simulations limited attention to only non-zero gaps between the particle and the wall. The recent work by Zeng *et al.* (2009) has extended the results to the limit of a particle touching and sliding on the wall in an otherwise quiescent fluid. The problem of a stationary particle in a wall-bounded shear flow at finite Reynolds number and varying distances from the wall, including the zero-gap limit, was also considered by Zeng *et al.* (2009). Thus, if we consider the superposition suggested by Krishnan & Leighton (1995) to apply even at finite Reynolds numbers, the shear and translation contributions have been established for varying distances from the wall (Zeng *et al.* 2009).

Here we first perform a series of fully resolved simulations of a spinning sphere in a quiescent fluid close to a flat wall. By systematically varying the gap between the particle and the wall, we are able to approach the limit of particle touching the wall. The rotational Reynolds number of the particle is also varied and thereby we numerically establish the rotational contribution to the drag and lift forces. Motivated by the theoretical results of Krishnan & Leighton, we computationally consider binary interactions of shear–translation, shear–rotation and translation–rotation in the finite-Reynolds-number regime. Combining these new simulation results with those of Zeng *et al.* (2009), a finite-Reynolds-number extension to the drag and lift superposition is proposed for the case of a particle in arbitrary translational and rotational motion in a wall-bounded linear shear flow.

2. Problem description

Consider a spherical particle of diameter d rotating at an angular velocity $\tilde{\Omega}$ about the z-axis and translating at a velocity $\tilde{V}_p$ parallel to the flat plate, which is located at a distance $\tilde{L}$ from the centre of the particle (see figure 1). The ambient flow approaching the particle is a linear shear flow, whose only non-zero velocity component is along the x-axis parallel to the wall. The shear flow can be written as $\tilde{U}(\tilde{y}) = \tilde{G}(\tilde{y} + \tilde{L})$, where $\tilde{G}$ is the dimensional shear rate of the ambient flow.

We choose the particle diameter d to be the length scale. We set the velocity scale to be $\tilde{V}$, which can be chosen to be the translational velocity of the particle ($\tilde{V}_p$), or the local shear flow velocity at the centre of the particle ($\tilde{G}\tilde{L}$) or the relative velocity.

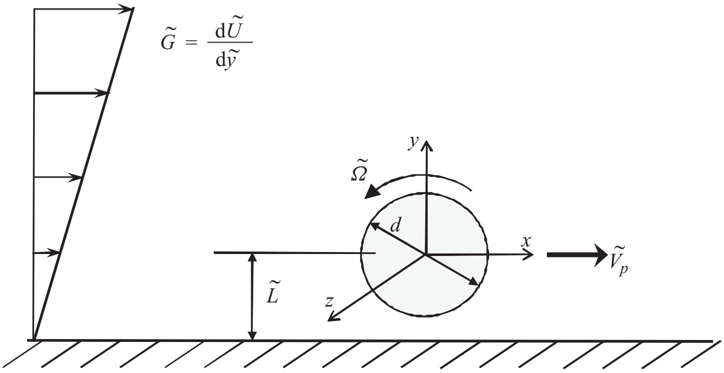

FIGURE 1. A schematic representation of a moving sphere in a wall-bounded linear shear flow and nomenclature used in this paper.

For now, we leave this definition unspecified. The time and pressure scales are defined accordingly. The resulting non-dimensional governing equations are as follows:

$$\left.\begin{aligned} \nabla \cdot \boldsymbol{u} &= 0, \\ \frac{\partial \boldsymbol{u}}{\partial t} + \boldsymbol{u}\cdot\nabla\boldsymbol{u} &= -\nabla p + \frac{1}{Re}\nabla^2\boldsymbol{u} + \boldsymbol{f}. \end{aligned}\right\} \tag{2.1}$$

Here we employ an immersed boundary technique in order to impose the appropriate velocity boundary conditions on the surface of the translating and rotating spherical particle, as it moves through a fixed Cartesian grid. The details of the immersed boundary technique and its accuracy will be discussed below. The local volume force, $\boldsymbol{f}$, arises from the immersed boundary technique and it enforces the motion of the solid body. This force is identically zero outside the particle and we recover the standard Navier–Stokes equation in the fluid.

The governing equations can be solved in a frame of reference fixed on the particle and in this frame the computational grid around the particle becomes time independent. In this translating frame, the ambient shear flow becomes $\tilde{G}(\tilde{y}+\tilde{L})-\tilde{V}_p$. When the particle motion is in the direction of shear flow (i.e. when $\tilde{G},\ \tilde{V}_p > 0$ or $\tilde{G},\ \tilde{V}_p < 0$), the ambient shear flow, as seen in the frame of reference translating with the particle, switches sign (reverses direction) at $\tilde{y}=(-\tilde{L}+\tilde{V}_p/\tilde{G})$. For the cases of a stationary particle in a shear flow ($\tilde{G} \neq 0,\ \tilde{V}_p=0$) or a translating particle in a quiescent medium ($\tilde{G}=0,\ \tilde{V}_p \neq 0$), there is no ambient flow reversal as seen by the particle. The corresponding boundary conditions on the left- and right-hand sides of the computational domain are entirely inflow or outflow. Only in the case of combined particle translation in a shear flow, which is being considered here, the ambient flow direction changes as $\tilde{y}$ increases above the wall. The left and right boundaries of the computational domain will then be partly inflow and partly outflow. Imposition of such mixed boundary conditions on individual faces of the computational domain poses challenge and thus computational results employing such mixed boundary conditions must be appropriately verified.

Instead, if computations were to be performed in a fixed laboratory frame of reference, the numerical methodology must be capable of handling the translational motion of the particle. If a body-fitted grid such as the one employed in Zeng *et al.* (2005, 2009) were to be used, then a complex time-dependent grid evolution will be required to accommodate the particle motion. With the immersed boundary approach, we can enforce the boundary conditions corresponding to a translating–rotating particle in a fixed Cartesian grid relatively easily. However, as will be discussed below, the computational cost associated with simulating the moving particle in a fixed laboratory frame is several times more than that associated with simulating a moving frame, where the particle remains fixed. Here, with the immersed boundary methodology, we will solve a few selected cases both in the moving and fixed reference frames. Comparing the results, the accuracy of the moving-frame simulations will be established.

If the location of the particle centre is given by $\boldsymbol{x}_p$, then the boundary conditions to be employed in the laboratory frame of reference are given as follows:

$$\boldsymbol{u} = \begin{cases} V_p \boldsymbol{e}_x - (\boldsymbol{x} - \boldsymbol{x}_p) \times 2\Omega \boldsymbol{e}_z & \text{for} \quad |\boldsymbol{x} - \boldsymbol{x}_p| \leqslant 1/2, \\ 2G(L + y)\boldsymbol{e}_x & \text{for} \quad |\boldsymbol{x} - \boldsymbol{x}_p| \rightarrow \infty, \\ 0 & \text{for} \quad y = -L, \end{cases} \tag{2.2}$$

where the terms without tilde indicate non-dimensional quantities ($V_p = \tilde{V}_p/\tilde{V}$, $G = (\tilde{G}d/2)/\tilde{V}$, $\Omega = (\tilde{\Omega}d/2)/\tilde{V}$) and $\boldsymbol{x} - \boldsymbol{x}_p$ is the position vector from the centre of the particle. The grid to be employed in the simulations is clustered near the particle to enhance resolution. In the case of laboratory-frame simulations, since the particle moves with respect to the grid, we need to employ a fine grid along a significant streamwise length of the computational domain. Such increased resolution over an extended region of the computational domain is at the expense of significant computational cost. In contrast, in the moving frame of reference with mixed boundary conditions at the left and right ends of the computational domain, the region of high resolution is confined to be only around the fixed particle. In all simulations, Neumann boundary conditions are employed at the top and side (lateral) boundaries. In the moving frame of reference, the boundary conditions (2.2) are modified accordingly.

In (2.1) the Reynolds number is defined as $Re = \tilde{V}d/\nu$. Several other velocity scales can be used in the definition of the Reynolds number. We can also define shear, translation, rotation and relative Reynolds numbers as

$$\left.\begin{aligned} &\text{Shear:} && Re_s = \frac{|\tilde{G}|\tilde{L}d}{\nu} = 2|G|LRe, \\ &\text{Translational:} && Re_t = \frac{|\tilde{V}_p|d}{\nu} = |V_p|Re, \\ &\text{Rotational:} && Re_\Omega = \frac{|\tilde{\Omega}|d^2}{\nu} = 2|\Omega|Re, \\ &\text{Relative:} && Re_r = \frac{|\tilde{G}\tilde{L} - \tilde{V}_p|d}{\nu} = |2GL - V_p|Re. \end{aligned}\right\} \tag{2.3}$$

2.1. *Numerical methodology*

A second-order accurate central difference scheme is used for the spatial discretization of the governing equations on a non-staggered Cartesian grid system. A fractional step method is used for the time advancement. In the advection–diffusion step, the nonlinear terms are treated explicitly using second-order Adams–Bashforth scheme and the diffusion terms are treated implicitly with the Crank–Nicolson scheme. The final divergence-free velocity is obtained at each time step with a pressure correction step. Pressure correction requires the solution of the pressure Poisson equation (Zang *et al.* 1994).

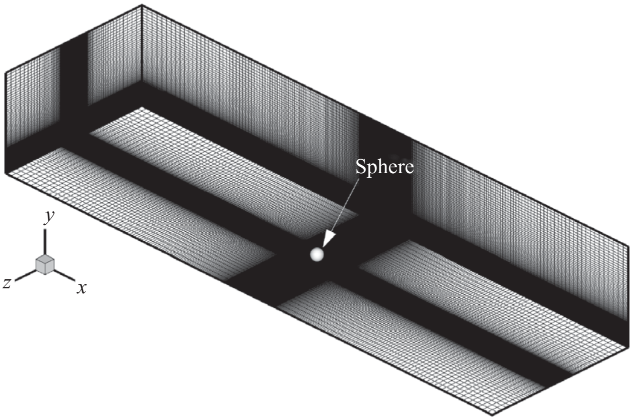

FIGURE 2. Stretched grid system around a sphere near a smooth wall. For the case shown, the number of grid points and domain sizes are $371\times129\times151$ and $[-25, 25]\times[-0.505, 8]\times[-7, 7]$.

In order to resolve the finite-sized spherical particle in the Cartesian grid, here we employ the immersed boundary technique following the implementation suggested by Uhlmann (2005). This direct forcing method allows the localized volume force, $\boldsymbol{f}$, applied in (2.1) to be computed explicitly at each time step. The volume forces and the transfer kernel function play an important role in transferring quantities between particle-related Lagrangian and fluid-related Eulerian grid points. Here we use the regularized delta function as the transfer kernel in which we use a three-point stencil (Roma, Peskin & Berger 1999). For the Lagrangian grid, a uniform distribution of points over the surface of the sphere is used (Saff & Kuijlaars 1997). These Lagrangian forcing points are employed over the entire surface and inside of the surface to form a multi-layer.

A non-uniform Cartesian grid employed in the simulations is shown in figure 2. The Eulerian grid points are clustered close to the wall along the wall-normal direction and clustered around the sphere along the spanwise direction. The clustering of points is important in order to achieve a high degree of resolution around the sphere in its representation in the immersed boundary method. In the immersed boundary region that embeds the sphere, a uniform Cartesian mesh of equal resolution along all three directions is used ($\Delta x = \Delta y = \Delta z$). This high-resolution region extends over $[-L, 1] \times [-1, 1]$ along the wall-normal and spanwise directions. In the case of a stationary particle centred about the origin in the computational frame of reference, the region of high resolution is limited over the streamwise direction and extends from $[-1, 1]$. When simulating a translating particle in a stationary laboratory frame of reference, first the streamwise extent of the computational domain needs to be long in order to accommodate the streamwise movement of the particle. Second, the streamwise extent of higher resolution is long and chosen to cover the entire trajectory of the particle, thus adding to the computational cost.

Outside this region of the uniform grid, a geometric grid stretching is used. Each successive grid spacing is progressively increased by a multiplicative factor α. The value of the stretch parameter α, the size of the computational domain and the number of grid points used to resolve one sphere diameter in the uniform grid region (N_p) dictate the number of grid points used. The overall grid resolution used in the simulations is up to $371 \times 301 \times 151$ points. The computational domain employed in the simulations extends over $[-25, 25] \times [-L, 8] \times [-7, 7]$ units along the streamwise,

	Number of grid	Domain size	$C_{D,r}$		$C_{L,r}$	
$1/\Delta x$	$N_x \times N_y \times N_z$	$L_x \times L_y \times L_z$	Value	Difference (%)	Value	Difference (%)
20	$193 \times 71 \times 97$	$[-25, 25] \times [-0.505, 8] \times [-7, 7]$	1.431	15.4	0.174	8.4
30	$257 \times 97 \times 129$	$[-25, 25] \times [-0.505, 8] \times [-7, 7]$	1.240	2.4	0.190	2.1
40	$371 \times 129 \times 151$	$[-25, 25] \times [-0.505, 8] \times [-7, 7]$	1.225	1.2	0.194	1.0
50	$431 \times 151 \times 177$	$[-25, 25] \times [-0.505, 8] \times [-7, 7]$	1.211	–	0.196	–

TABLE 1. Grid resolution test for the case of $V_P = -1$, $L = 0.505$, $Re_s = 100$. We present the drag and lift coefficients for different resolutions. The finest grid results are taken to be the baseline and percentile differences between with the finest and the coarse grids defined as difference $= |(\phi_{coarser} - \phi_{finest})/\phi_{finest}| \times 100\,(\%)$ are presented.

wall-normal and spanwise directions. The choice of the domain is consistent with those used in Zeng *et al.* (2009), who established the adequacy of the computational domain. The simulation results to be discussed here typically involve 40 grid points resolving one particle diameter in the high-resolution region. The overall number of grid points for such a simulation varies from $371 \times 129 \times 151$ grid points along the streamwise, wall-normal and spanwise directions (for $L \sim 0.5$) to $371 \times 301 \times 151$ grid points (for $L = 4$). The increased resolution for $L = 4$ in the wall-normal direction is due to the larger region of high resolution. Only for the case of a particle under pure rotation (without translation or ambient shear to be described in § 3.1) we use a larger domain that extends in the wall-normal direction $[-L, 25]$ in order to minimize the effect of the finite domain size.

2.2. *Grid independence and validation*

First we establish the number of grid points needed within the context of immersed boundary method in order to achieve adequate resolution of the spherical particle. As a test we consider the case of a particle translating along the negative x-direction in a linear shear flow. The particular case considered is characterized by $V_p = \tilde{V}_p/(\tilde{G}\tilde{L}) = -1$, $L = 0.505$ and $Re_s = 100$. Four different levels of resolution are employed ($1/\Delta x = 20$, 30, 40 and 50). The drag and lift coefficients based on relative velocity ($C_{D,r} = \tilde{F}_x/((\pi/8)\rho(\tilde{G}\tilde{L} - \tilde{V}_p)^2 d^2)$ and $C_{L,r} = \tilde{F}_y/((\pi/8)\rho(\tilde{G}\tilde{L} - \tilde{V}_p)^2 d^2)$) for the different simulations are presented in table 1. Also presented are the domain size and the number of grid points used in these simulations. Based on the above results, the bulk of the results to be presented (unless otherwise stated) are obtained with a resolution of $1/\Delta x = 40$.

Here, the results of Zeng *et al.* (2005, 2009), obtained using the higher order accurate spectral element methods, will be used as the benchmark in validating the present numerical approach. Rigorous testing and validation of the spectral element approach have already been presented in these earlier works. Figure 3 shows the comparison of drag and lift coefficients for several cases of stationary particle in a linear wall-bounded shear flow and several cases of particle translating parallel to a flat wall in a quiescent fluid. In figures 3(*a*) and 3(*b*) we present the drag and lift coefficients, defined as

$$C_{D,s} = \frac{\tilde{F}_x}{\frac{\pi}{8}\rho\tilde{G}|\tilde{G}|\tilde{L}^2 d^2} \quad \text{and} \quad C_{L,s} = \frac{\tilde{F}_y}{\frac{\pi}{8}\rho\tilde{G}^2\tilde{L}^2 d^2}, \tag{2.4}$$

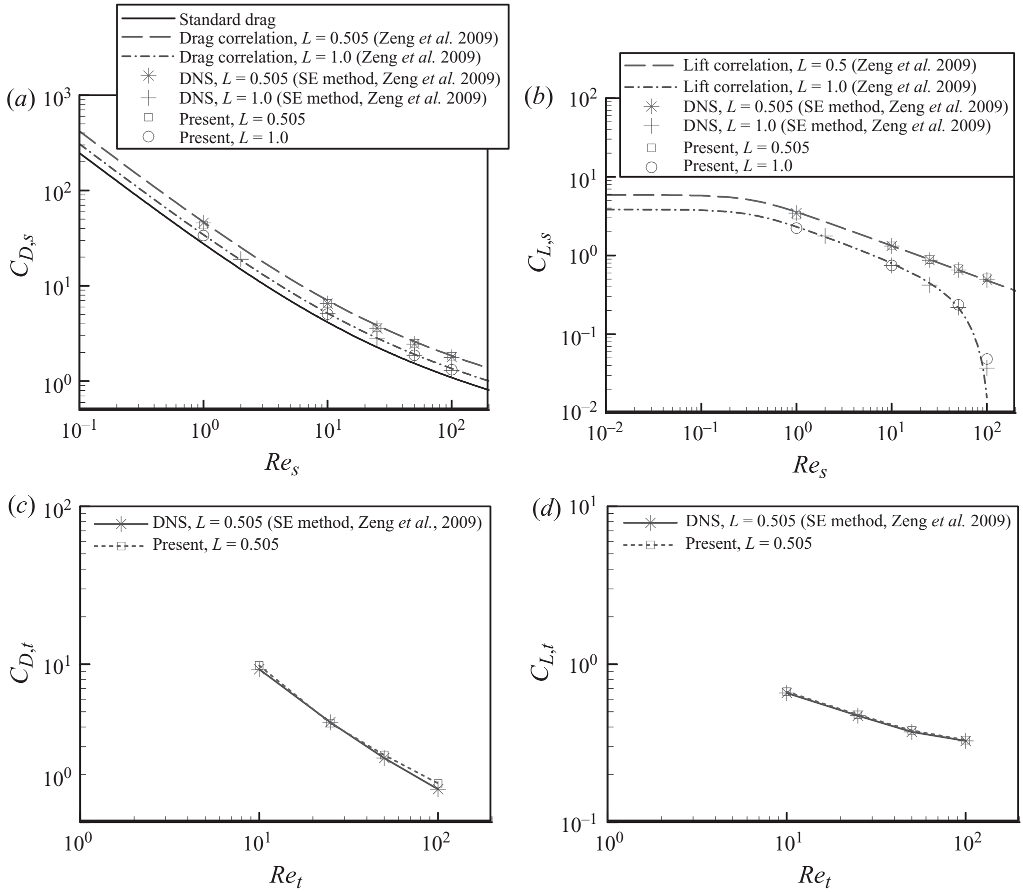

FIGURE 3. Comparison of drag and lift coefficients obtained with the present code against those obtained with the spectral element methodology of Zeng *et al.* (2005). (*a*) Drag and (*b*) lift for a stationary particle in a linear wall-bounded shear flow. (*c*) Drag and (*d*) lift for a translating particle in a quiescent fluid.

for the case of a stationary particle in a linear wall-bounded shear flow and compare results with those of Zeng (2007). The results for both the case of a particle almost touching the wall ($L = 0.505$) and the case of a particle away from the wall ($L = 1.0$) are compared over a range of Reynolds numbers. Also shown is the standard drag correlation (Schiller & Naumann 1933). In the immersed boundary approach, the sphere is resolved with 40 grid points across one particle diameter (i.e. $1/\Delta x = 40$). The comparison is generally quite good and the spectral element results are well recreated with the present immersed boundary approach. Some difference can be observed in figure 3(*b*) for the highest Reynolds number case. Note that the lift coefficient is plotted on a log scale and thus the difference between the two approaches contributes to differences when the lift force is very small.

The corresponding translation-induced force coefficients for the case of a particle in translation parallel to a wall are defined as

$$C_{D,t} = \frac{\tilde{F}_x}{\dfrac{\pi}{8}\rho \tilde{V}_p |\tilde{V}_p| d^2} \quad \text{and} \quad C_{L,t} = \frac{\tilde{F}_y}{\dfrac{\pi}{8}\rho \tilde{V}_p^2 d^2}. \tag{2.5}$$

Re_s	$V_p = (\tilde{V}_p/\tilde{G}\tilde{L})$	L	$1/\Delta x$	Method	$C_{D,s}$	$C_{L,s}$
10	−1.0	1	30	Moving frame	12.159	1.336
				Laboratory frame	12.164	1.337
10	0.5	1	30	Moving frame	2.316	0.409
				Laboratory frame	2.318	0.411
100	0.5	1	30	Moving frame	0.581	0.190
				Laboratory frame	0.584	0.192

TABLE 2. Comparison between the moving frame and laboratory frame simulations.

Drag and lift coefficients obtained from the present numerical approach are compared with those from the spectral element simulations for the case of $V_p = \tilde{V}_p/|\tilde{V}_p| = -1$. The comparison is quite good even for the extreme case of close proximity between the particle and the wall. Additional validation of the present numerical results is presented in § 3, where appropriate comparisons are made with low-Reynolds-number theories.

We now establish the appropriateness of simulations performed in the frame of reference attached to a translating particle in a linear shear flow by comparing results with those performed in a laboratory frame where the particle moves through the fixed Cartesian grid. Here we refer to the former as the ‘moving-frame simulation’ and the latter as the ‘laboratory-frame simulation’. Table 2 presents a comparison of the two simulations for a range of conditions. The small differences in results can be attributed to the different streamwise extent of the computational domains used in the two approaches and also to differences in the implementation of the streamwise boundary conditions.

3. Results

3.1. *Particle rotation in a quiescent fluid near a flat wall*

Here we plan to complement our current understanding of the shear-induced forces on a stationary particle in a linear shear flow and the translation-induced forces on a particle moving parallel to a wall in a quiescent fluid. We will perform a systematic investigation of a particle spinning about the z-axis in a quiescent fluid. By performing well-resolved simulations of this problem for rotational Reynolds numbers over the range $1 \leqslant Re_\Omega \leqslant 100$ and for the following distances from the wall, $L = 0.505$, 0.525, 0.55, 0.625, 0.75, 1, 2 and 4, we will develop a better understanding of the pure rotation-induced forces on a particle in the presence of a nearby wall.

3.1.1. *Flow features*

We examine the flow induced by the rotating particle by plotting streamlines, pressure and vortical structures around the particle for $Re_\Omega = 10$ and 100 in figures 4–7. In figures 4 and 5 the streamlines and pressure contours are plotted on the symmetry plane ($z = 0$) for three distinct particle locations ($L = 0.505$, 1 and 4), and the particle rotation is counterclockwise.

In figure 4 several prominent features can be observed in the streamlines. In the immediate vicinity of the sphere on the symmetry plane, we observe the streamlines to spiral out in the counterclockwise direction. The fluid rotation about the z-axis due to the spinning sphere causes a low-pressure region around the particle (see figure 5). This low-pressure draws fluid along the spanwise direction inwards towards the sphere,

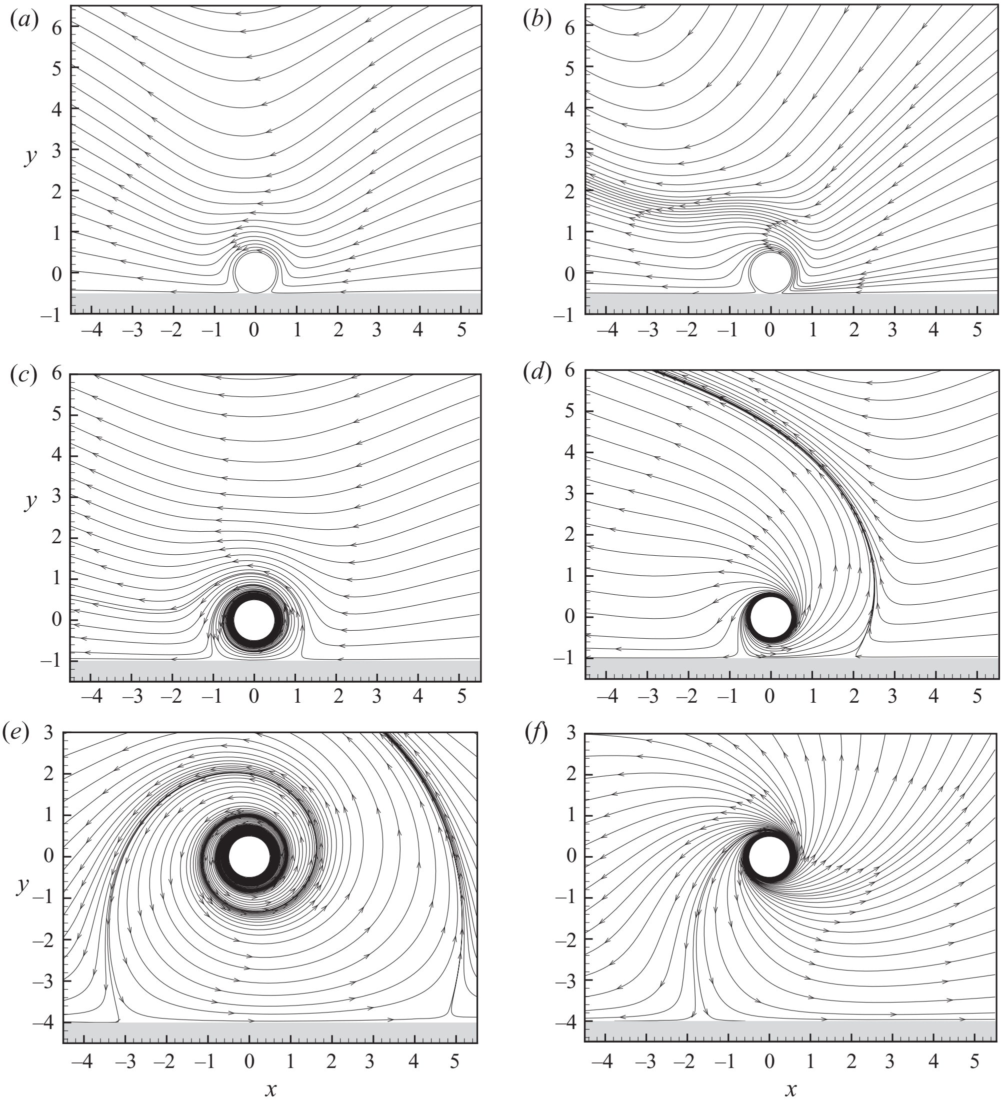

FIGURE 4. Streamline patterns on the symmetry plane ($z = 0$) of a purely rotating particle. (*a*), (*c*) and (*e*) $Re_{\Omega} = 10$; (*b*), (*d*) and (*f*) $Re_{\Omega} = 100$. (*a*) and (*b*) $L = 0.505$; (*c*) and (*d*) $L = 1$; (*e*) and (*f*) $L = 4$.

which is spun outwards along the symmetry plane ($z = 0$). This is a finite-Reynolds-number feature of the flow. In the zero-Reynolds-number limit, the flow around a spinning particle (often termed Rotlet) is purely circumferential and the pressure is uniform. At finite *Re*, the radial outflow exists even in the absence of the wall and gets modified as the particle gets closer to the wall. The spiralling flow pattern on the symmetry plane results in two hyperbolic fixed points on the wall, which are clearly visible as the gap between the particle and the wall increases. Without the wall, flow around the particle will be perfectly axisymmetric about the z-axis. The wall breaks the axisymmetry and a spinning particle will experience higher shear stress in the gap region below the particle than above it. The broken axisymmetry thus results in a non-zero drag force, and for a particle rotating counterclockwise (positive z-rotation), this force is directed in the negative x-direction.

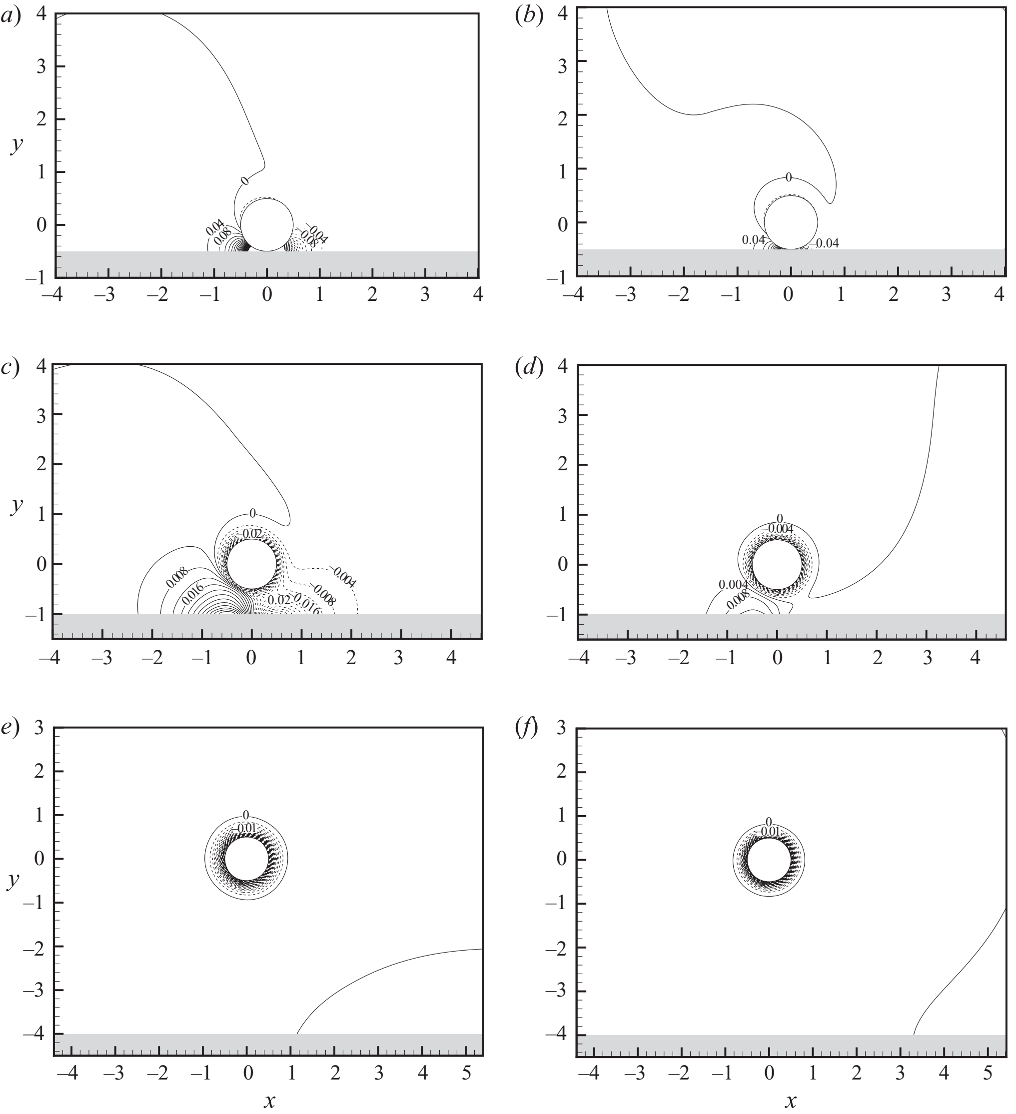

FIGURE 5. Pressure distributions on a symmetric plane ($z=0$) of a purely rotating particle. (*a*), (*c*) and (*e*) $Re_\Omega = 10$; (*b*), (*d*) and (*f*) $Re_\Omega = 100$. (*a*) and (*b*) $L = 0.505$ (p : [–1, 1], $\Delta p = 0.04$); (*c*) and (*d*) $L = 1$ (p : [–0.1, 0.1], $\Delta p = 0.004$); (*e*) and (*f*) $L = 4.0$ (p : [–0.1, 0], $\Delta p = 0.002$).

Contours of pressure for different gaps and Re_Ω are shown in figure 5. Here we used the far-field pressure as the reference pressure. When the particle is almost sitting on the wall ($L = 0.505$), as shown in figures 5(*a*) and (*b*), high- and low-pressure regions occur to the left and the right of the particle, respectively. The high pressure is due to the fluid being squeezed into the small gap between the particle and the wall. The integrated pressure-induced streamwise force on the particle is directed in the positive x-direction. Nevertheless, the distribution of pressure around the particle is such that the pressure contribution to the drag force is much weaker than that from the shear stress and thus the net drag force on the particle is towards the negative x-direction. As the gap increases, the effect of the wall weakens. For $L = 4$, the high- and low-pressure regions in the gap are not discernible and only a low-pressure

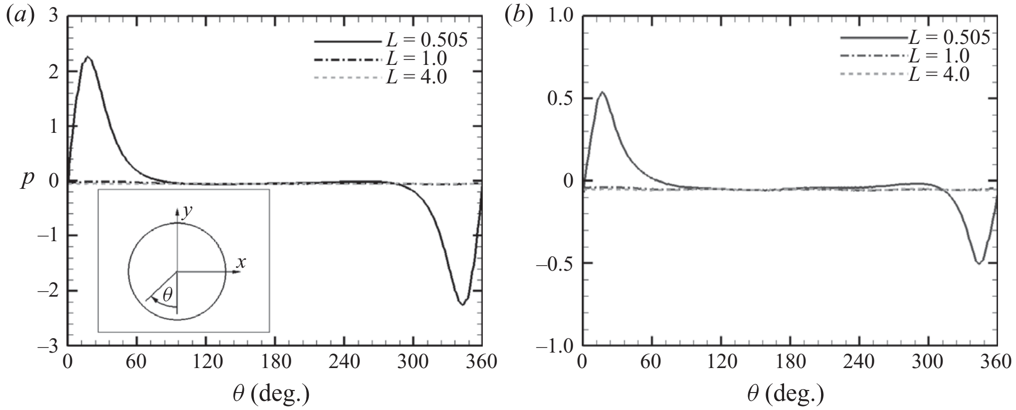

FIGURE 6. Surface pressure distribution as a function of angle on the $z = 0$ plane for different gap values between the particle and the wall: (*a*) $Re_\Omega = 10$; (*b*) $Re_\Omega = 100$.

region is seen distributed around the particle. As seen in figure 4 the lower pressure draws fluid inwards towards the particle along the spanwise (z) direction and spirals it out along the radial direction. To further clarify the pressure effect, we present the pressure distribution on the particle along the symmetry plane in figure 6. At $L = 0.505$, relatively strong pressure variation around the particle can be observed. For $Re_\Omega = 10$ and 100, even though the magnitude of peak pressure is different, the highest and lowest pressures occur at similar angles of $\theta_{HP} \approx 17°$, $\theta_{LP} \approx 343°$. At large gap values ($L = 1$ and 4), the pressure variation around the particle is much smaller than for $L = 0.505$.

Figure 7 shows the vortical structures around the rotating particle for three selected distances from the wall ($L = 0.505$, 1 and 4). In this figure the left column (*a*, *c*, *e*) and the right column (*b*, *d*, *e*) represent $Re_\Omega = 10$ and 100, respectively. The vortex structures are identified by plotting contours of swirling strength ($\lambda_{ci} = 0.1$), defined as the imaginary part of the complex eigenvalues of the local velocity gradient tensor (Zhou *et al.* 1999; Chakraborty, Balachandar & Adrian 2005). At the lower Reynolds number ($Re_\Omega = 10$), the vortex structures appear as circular patches on either side of the particle. At the higher Reynolds number of $Re_\Omega = 100$, we can see an additional pair of 'doughnut-shaped' symmetric vortex structures appearing on either sides of the sphere. At both Reynolds numbers if the particle is located sufficiently away from the wall ($L = 4$), then the vortex structures are nearly axisymmetric, suggesting the wall effect on the particle to be nearly negligible at this distance. As the particle approaches the wall, the vortex structures are initially distorted and, as the gap approaches zero, the distortion increases and the vortex structures appear to be somewhat broken.

3.1.2. *Drag force*

In the present case, rotational drag, lift and moment coefficients on the sphere are defined as follows:

$$C_{D,\Omega} = \frac{-\tilde{F}_x}{\frac{\pi}{32}\rho\tilde{\Omega}|\tilde{\Omega}|d^4}, \quad C_{L,\Omega} = \frac{\tilde{F}_y}{\frac{\pi}{32}\rho\tilde{\Omega}^2 d^4} \quad \text{and} \quad C_{M,\Omega} = \frac{-\tilde{T}_z}{\frac{\pi}{64}\rho\tilde{\Omega}|\tilde{\Omega}|d^5}. \qquad (3.1)$$

The drag coefficients obtained from the simulations are plotted as symbols in figure 8(*a*) as a function of L in log-linear scale for different Reynolds numbers. The rapid increase in drag coefficient as the wall is approached is clear. For small and large values of the gap, the results can be compared with the lubrication theory

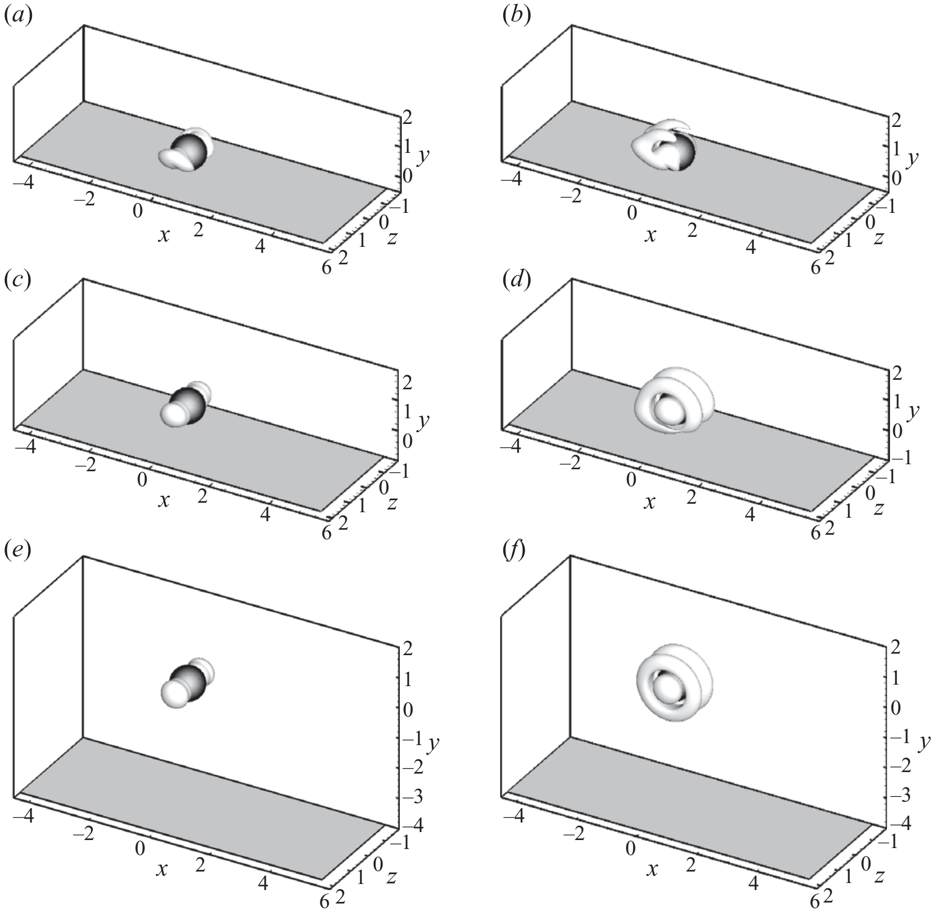

FIGURE 7. Vortical structures of a purely rotating particle close to a wall (swirling strength $\lambda_{ci} = 0.1$). (*a*), (*c*) and (*f*) $Re_\Omega = 10$; (*b*), (*d*) and (*f*) $Re_\Omega = 100$. (*a*) and (*b*) $L = 0.505$; (*c*) and (*d*) $L = 1.0$; (*e*) and (*f*) $L = 4.0$.

of Goldman *et al.* (1967*a*), and with results obtained from the method of reflection, respectively. Here we rewrite the drag coefficient as a resistance coefficient as defined in Goldman *et al.* (1967*a*):

$$f_{x,\Omega} = \frac{-2\tilde{F}_x}{3\pi\mu\tilde{\Omega}d^2} = \frac{Re_\Omega C_{D,\Omega}}{48}. \tag{3.2}$$

The low-Reynolds-number behaviour of the resistance coefficient for small-gap (from lubrication theory) and for large-gap (from method of reflections) limits can be expressed in terms of the non-dimensional gap ($\varepsilon = 2L - 1$) as (Goldman *et al.* 1967*a*)

$$f_{x,\Omega} \sim -\frac{2}{15}\ln\varepsilon - 0.2526 \text{ for } \varepsilon \ll 1 \text{ and } f_{x,\Omega} \sim \frac{1}{8}\left(\frac{1}{1+\varepsilon}\right)^4\left(1 - \frac{3}{8(1+\varepsilon)}\right) \text{ for } \varepsilon \gg 1. \tag{3.3}$$

Experiments were carried out to measure both the translational and rotational velocities of a sphere moving parallel to a wall (Małysa & van de Ven 1986). According to their measurements, Goldman *et al.*'s (1967*a*) lubrication theory predicts

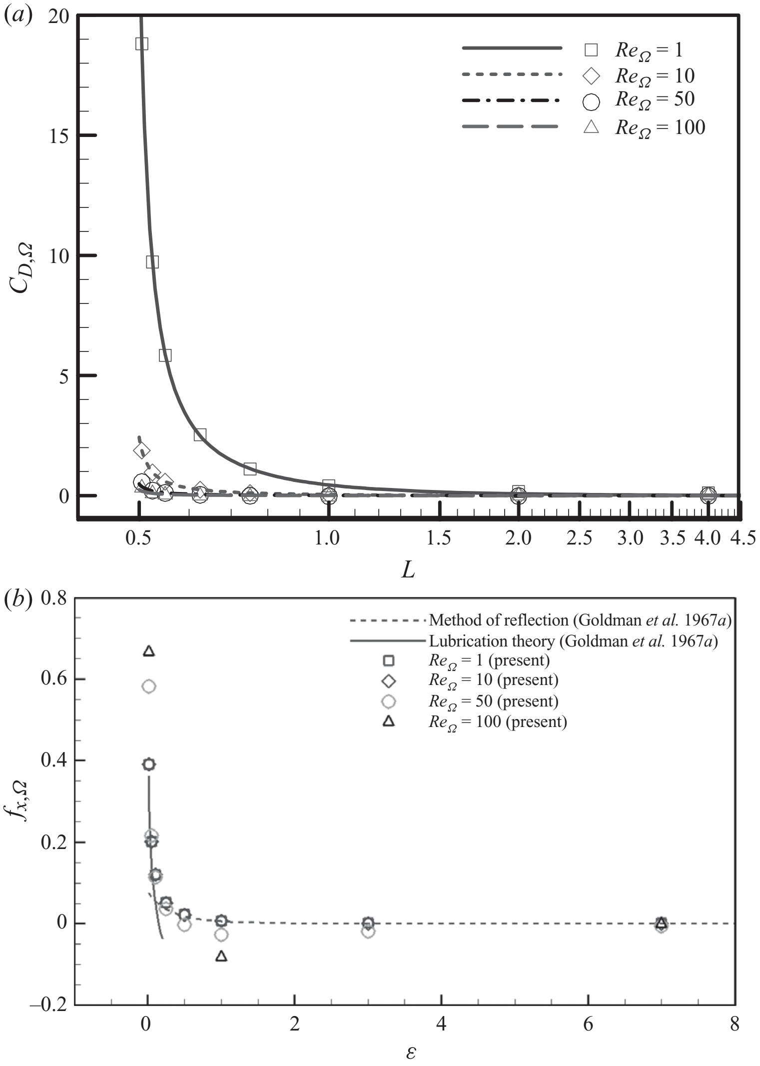

FIGURE 8. (*a*) Drag coefficients of a rotating particle for different rotation Reynolds numbers and gap distances. Symbols: results from the numerical simulations; lines: from (3.4). (*b*) Dimensionless resistance coefficient compared with the low-Reynolds-number theories.

well for small gaps of $\varepsilon < 0.04$ and the method of reflections is accurate for large gap values of $\varepsilon > 0.3$. However, at intermediate gaps, both theories cannot accurately predict the force on the sphere.

In figure 8(*b*) the resistance coefficient computed from the simulations are plotted as a function of ε. Also plotted are the results of the lubrication theory and the method of reflections. At all gaps considered, the drag force as expressed in terms of resistance coefficient is nearly independent of Reynolds number up to about $Re_\Omega \sim 10$. The agreement with the low-Reynolds-number theories is quite good at both the small- and large-gap limits. At small gaps, the resistance coefficient increases with Re_Ω, but at intermediate values of the gap, the resistance coefficient decreases with Re_Ω. At large gaps, the drag force is nearly zero and above a certain Reynolds number the approach seems to be from below. Thus, above a certain Reynolds number, the drag force becomes negative at intermediate values of the gap. This behaviour is similar

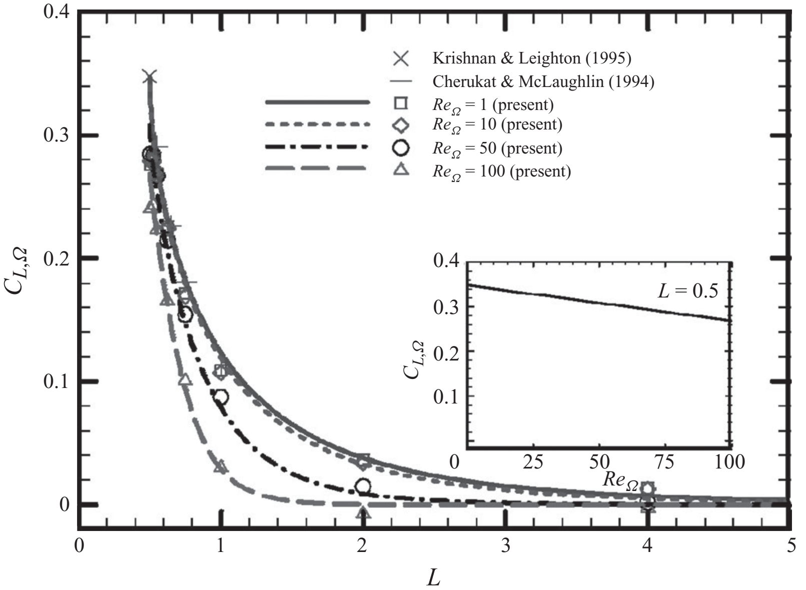

FIGURE 9. Lift coefficients of a rotating particle for different rotation Reynolds numbers and gap distances. Symbols and lines are the results from numerical simulations and (3.5), respectively. The inset shows results for the case of particle touching the wall for varying Reynolds number. These results are extrapolated from the numerical simulations to $L = 0.5$.

to that observed for the cases of a wall-bounded shear flow over a particle and of a translating particle parallel to a wall in a quiescent fluid (Zeng *et al.* 2009). In both these cases, at intermediate values of gap, the drag force on the particle was observed to be lower than what would be in the absence of the wall. Such reduction was also identified in the theoretical results of Vasseur & Cox (1976), who explained this reduction in terms of a potential contribution induced by an inflow and outflow from the wall boundary layer. A similar mechanism can be expected to be active in the present case of a spinning particle at sufficient wall–particle separation.

Here we obtain a simple correlation for the drag coefficient for the spinning sphere in the proximity of a wall:

$$C_{D,\Omega}(L, Re_\Omega) = \frac{0.2425}{Re_\Omega}(L^2 - 0.4252L - 0.02743)^{-1}. \tag{3.4}$$

In figure 8(*a*), the calculated drag using (3.4) is plotted as lines over the *Re* and *L* range considered in the simulations. The above expression provides a good approximation for the numerical results over this range. Also, the difference between the above expression and the results of Goldman *et al.* (1967*a*) at low Re_Ω is sufficiently small that (3.4) can be taken to be adequate. However, note that in the low-Reynolds-number limit, the above correlation does not capture the logarithmic singularity as $L \rightarrow 1/2$ and the L^{-4} decay for large separation, as indicated in (3.3). An improved expression that obeys these limits can be constructed, but it is observed to be far more complex. For $Re < 100$ and $0.505 \leqslant L \leqslant \infty$, the above simpler expression is observed to be quite accurate.

3.1.3. *Lift force*

In figure 9 the lift coefficient evaluated from the simulations is plotted as a function of *L* for different Reynolds numbers. In the limit of particle touching the wall ($L = 0.5$)

and $Re_\Omega \to 0$, the asymptotic theory of Krishnan & Leighton shows that $C_{L,\Omega} \to 0.348$. Similarly, the asymptotic analysis of Cherukat & McLaughlin can be used to obtain $C_{L,\Omega}$ as a function of L in the limit of small Reynolds number (see figure 2 in Krishnan & Leighton 1995). This low-Reynolds-number result can be fit well with the following expression: $C_{L,\Omega}(L, Re_\Omega \to 0) = 0.348[1 + \tanh(-0.767(2L-1)^{0.563})]$. The results from the low-Reynolds-number asymptotic analysis are also plotted in figure 9 as symbols and the agreement with the computational results of $Re_\Omega = 1$ is very good. This provides additional validation for the adequacy of present numerical resolution and the size of the computational domain.

The rotation-induced lift force falls off rapidly as the particle position moves away from the wall. The sequence of simulation results for small L can be extrapolated to obtain the lift force on a particle sitting on the wall. The inset in figure 9 shows $C_{L,\Omega}(L = 1/2, Re_\Omega)$ as a function of Re_Ω, and a good fit for this Reynolds number dependence is given by $0.348 - 0.000795\, Re_\Omega$ and it is accurate for $Re_\Omega \leqslant 100$. It can be readily seen that at all separations from the wall, for small Reynolds numbers, $C_{L,\Omega}$ is nearly a constant only weakly dependent on Re_Ω. This is in contrast to the drag coefficient, $C_{D,\Omega}$, which has a Re_Ω^{-1} behaviour at low Reynolds numbers. The following expression for the lift coefficient has been found to be effective in describing the simulation results:

$$C_{L,\Omega}(L, Re_\Omega) = (0.348 - 0.000795 Re_\Omega)\big[1 + \tanh\big(\big(-0.767 - 0.00018 Re_\Omega^{1.785}\big) \times (2L-1)^{0.563+0.00317 Re_\Omega}\big)\big] \quad \text{for } Re_\Omega \leqslant 100. \tag{3.5}$$

Note that it precisely reduces to the correct behaviours both in the limit of low Reynolds number and in the limit of the particle touching the wall.

3.1.4. *Moment coefficient*

Following Goldman *et al.* (1967*a*), the torque on the particle can be expressed in terms of a rotational resistance coefficient as

$$t_{z,\Omega} = \frac{-\tilde{T}_z}{\pi \mu \tilde{\Omega} d^3} = \frac{Re_\Omega C_{M,\Omega}}{64}. \tag{3.6}$$

In figure 10(*a*) we present the moment coefficient, $C_{M,\Omega}$, obtained from numerical simulations plotted as a function of L in log–log scale for different values of the rotational Reynolds number. The low-Reynolds-number behaviour of $t_{z,\Omega}$ for small gaps is given by the lubrication theory and, for large gaps, it is given by the method of reflections. Goldman *et al.* (1967*a*) have expressed $t_{z,\Omega}$ in terms of the non-dimensional gap as

$$t_{z,\Omega} \sim \frac{2}{5}\ln\varepsilon - 0.3817 \quad \text{for} \quad \varepsilon \ll 1 \quad \text{and} \quad t_{z,\Omega} \sim -\left(1 + \frac{5}{16(1+\varepsilon)^3}\right) \quad \text{for} \quad \varepsilon \gg 1. \tag{3.7}$$

Figure 10(*b*) shows $t_{z,\Omega}$ obtained from the simulations plotted as a function of ε on a linear scale. Also plotted are the results of the lubrication theory and the method of reflections. Over the entire range of gap considered, $t_{z,\Omega}$ is observed to be nearly independent of Reynolds number provided Re_Ω is less than about 10. The agreement with the low-Reynolds-number theories is quite good at both the small- and large-gap limits. The change in the behaviour of $t_{z,\Omega}$ with Reynolds number is qualitatively similar to that observed for the resistance coefficient shown in figure 8(*b*). We observe the computed torque values at small separations to be more sensitive

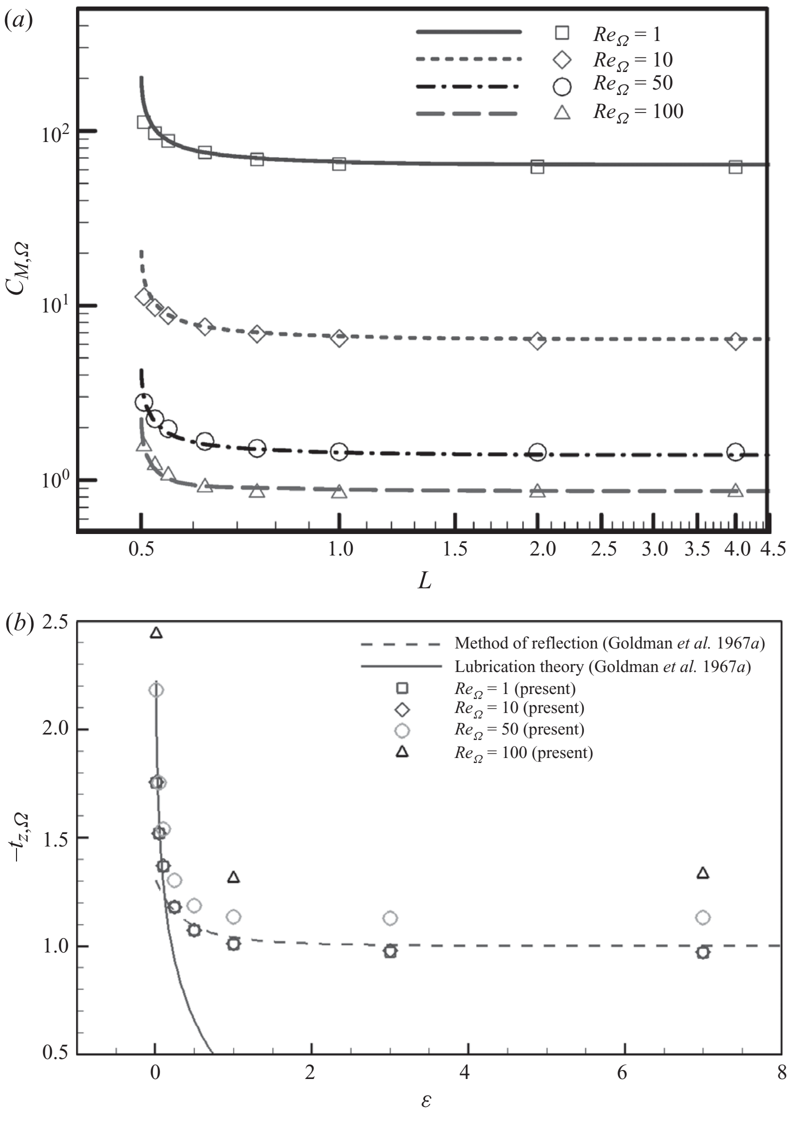

FIGURE 10. (*a*) Momentum coefficients and (*b*) dimensionless torque acting on a rotating particle for different Reynolds numbers and gaps between the particle and the wall.

than the force components. An expression for the moment coefficient of a particle undergoing rotational motion is given in (A 1) in the appendix. The expression is shown in figure 10(*a*) as lines and can be seen to well approximate the numerical results over the entire range of *Re* and *L* considered in this study.

3.1.5. *Comparison of shear, translation and rotation forces*

We compare the relative importance of the shear-, translation- and rotation-induced drag and lift forces in the limiting case of a particle in contact with the wall. Figure 11 shows the drag and lift coefficients for the three different cases plotted as a function of their respective Reynolds number. The definition of the shear-, translation- and rotation-induced force coefficients are given in (2.4), (2.5) and (3.1). Figure 11(*a*) shows a comparison of the three drag coefficients and all of them monotonically

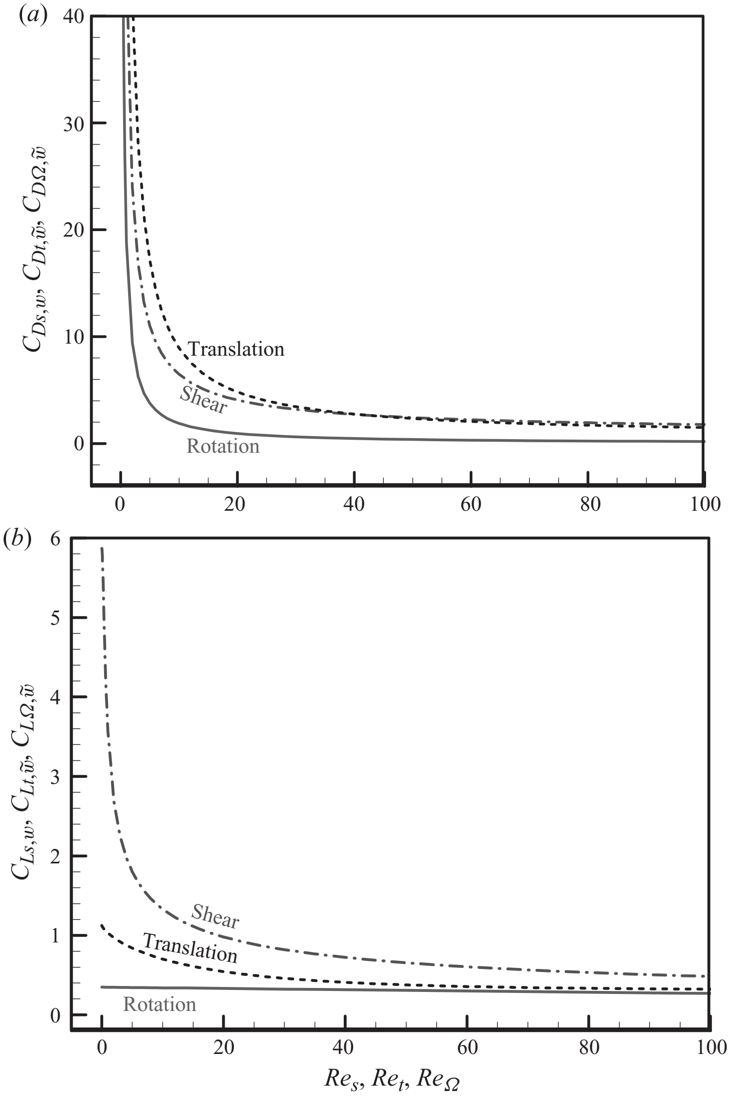

FIGURE 11. Forces due to shear flow, translation and rotation motion of a particle in contact with a wall. (*a*) Drag and (*b*) lift coefficients. Note that in the case of translation and rotation, the drag coefficients are for $L = 0.505$.

decrease with Re. It is clear that the rotation-induced drag is the weakest of the three. We can see that below a critical Reynolds number of about 42, translation-induced drag is larger than shear-induced drag. On the other hand, shear-induced drag becomes dominant beyond this Reynolds number. For the cases of a particle either in translation or in rotation, the drag force on the particle has a logarithmic singularity and becomes infinite when the particle comes into contact with the wall. But in reality the drag force on the particle will remain finite, since roughness of the particle and the wall will limit the effective gap to be non-zero. In figure 11(*a*) the results for translation and rotation are for a small separation of $L = 0.505$.

The Reynolds number dependence of the shear- and translation-induced drag coefficients for the general case of a particle close to a flat wall were presented in

Zeng *et al* (2009). The corresponding rotational drag expression is given in (3.4). These correlations reduce to the following relations in the limit of a particle touching the wall (or nearly touching the wall in the case of particle translation or rotation). Here and henceforth the letter '*w*' in the subscript for drag and lift coefficients indicate that the values are applicable strictly in the limit of particle touching the wall. While the letter '$\tilde{w}$' in the subscript indicates that the correlation is for almost touching the wall and in the present paper we arbitrarily choose $L=0.505$ to be sufficiently close to the wall. Thus, the correlations with '$\tilde{w}$' in the subscript are subject to change if a different value of particle-to-wall separation is considered:

$$\left.\begin{aligned} C_{Ds,w} &= \frac{40.81}{Re_s}\left(1+0.104Re_s^{0.753}\right), \\ C_{Dt,\tilde{w}} &= C_{Dt}(Re_t, L=0.505) = \frac{81.96}{Re_t}\left(1+0.01Re_t^{0.959}\right), \\ C_{D\Omega,\tilde{w}} &= C_{D\Omega}(Re_\Omega, L=0.505) = \frac{18.84}{Re_\Omega}. \end{aligned}\right\} \tag{3.8}$$

From figure 11(*b*) it is clear that the shear-induced lift is the strongest of the three and rotation-induced lift is the weakest. For instance, in the limit of small Reynolds number, the shear-induced lift coefficient is 5.87, while that due to translation is more than 5 times smaller at 1.12, and the rotation-induced lift coefficient is more than 16 times smaller at 0.348 (Krishnan & Leighton 1995). Equation (3.5) gives the Reynolds number behaviour of rotational lift coefficient and the corresponding correlations for the shear and translational lift coefficients have been obtained in Zeng *et al.* (2009) as

$$\left.\begin{aligned} C_{Ls,w} &= \frac{3.663}{\left(Re_s^2+0.1173\right)^{0.22}}, \\ C_{Lt,\tilde{w}} &= 0.313+0.812\exp\left(-0.125Re_t^{0.77}\right), \\ C_{L\Omega,\tilde{w}} &\approx 0.348-0.000795\,Re_\Omega. \end{aligned}\right\} \tag{3.9}$$

As indicated by the above expressions, shear-induced lift coefficient rapidly decreases at small Reynolds numbers, while for the translation-induced lift coefficient, the decay rate is modest. In contrast, the rotation-induced lift is nearly independent of Re_Ω at small Reynolds numbers. Thus, with increasing Reynolds number, the three different lift coefficients approach each other. But over the entire Reynolds number range considered here, the shear lift remains the strongest.

3.2. *Superposition at finite Re*

3.2.1. *Lift superposition*

The low-Reynolds-number results of Krishnan & Leighton (1995) for a particle rotating and translating parallel to a flat wall in a shear flow can be recast in the following form for the lift coefficient:

$$C_{L,w}(Re\to 0) = \frac{\tilde{F}_y}{\frac{\pi}{8}\rho d^2\tilde{V}^2} = \frac{2}{\pi}\left[\lambda_1 G^2+\lambda_2 V_p^2+\lambda_3\Omega^2+\lambda_4 G V_p-\lambda_5 G\Omega-\lambda_6 V_p\Omega\right], \tag{3.10}$$

where the first three terms on the right are the shear, translation and rotation contributions to lift and the latter three are shear–translation, shear–rotation and translation–rotation binary coupling contributions to lift. Krishnan & Leighton (1995) obtained the constants to be $\lambda_1 = 9.257$, $\lambda_2 = 1.755$, $\lambda_3 = 0.546$, $\lambda_4 = -9.044$, $\lambda_5 = 1.212$ and $\lambda_6 = -2.038$. Note that the velocity scale ($\tilde{V}$) remains unspecified, and it can be chosen to be any one of $\tilde{G}d/2$, $\tilde{V}_p$ or $\tilde{\Omega}d/2$. Suppose if we choose $\tilde{V} = \tilde{G}d/2$, then non-dimensional shear becomes $G = 1$ and the other two non-dimensional quantities are $V_p = 2\tilde{V}_p/(\tilde{G}d)$ and $\Omega = \tilde{\Omega}/\tilde{G}$. However, this scaling becomes inappropriate in the absence of shear. The advantage of the above equation is that it remains applicable even in the limit when some of the mechanisms are absent. Here we will assume the above superposition to hold qualitatively even at finite Reynolds numbers and propose the following form for the lift coefficient:

$$\left.\begin{aligned} C_{L,w} &= C_{Ls,w}G^2 + C_{Lt,w}V_p^2 + C_{L\Omega,w}\Omega^2 + \frac{2\lambda_4}{\pi}\frac{C_{Ls,w}C_{Lt,w}}{C_{Ls,w0}C_{Lt,w0}}GV_p\, f_{st}\left(Re_s, \frac{V_p}{G}\right) \\ &-\frac{2\lambda_5}{\pi}\frac{C_{Ls,w}C_{L\Omega,w}}{C_{Ls,w0}C_{L\Omega,w0}}\Omega G\, f_{s\Omega}\left(Re_s, \frac{\Omega}{G}\right) - \frac{2\lambda_6}{\pi}\frac{C_{Lt,w}C_{L\Omega,w}}{C_{Lt,w0}C_{L\Omega,w0}}V_p\Omega\, f_{t\Omega}\left(Re_t, \frac{\Omega}{V_p}\right). \end{aligned}\right\} \tag{3.11}$$

When only one lift mechanism is active with the other two mechanisms being absent, the last three binary coupling terms are identically zero. Depending on whether shear ($V_p = 0$ and $\Omega = 0$), translation ($G = 0$ and $\Omega = 0$) or rotation ($G = 0$ and $V_p = 0$) is active, respectively, the first, second or third term on the right makes the only non-zero contribution. Note that positive Ω here corresponds to counterclockwise rotation and is opposite to the convention adopted in Krishnan & Leighton (1995). This contributes to the minus signs in the last two coupling terms in (3.11).

The assumed coupling terms are motivated by their low-Reynolds-number form. For example, the lift contribution from shear–translation coupling is assumed to be proportional to $C_{Ls,w}C_{Lt,w}GV_p$ and any deviation from this is taken into account with the function f_{st}. Similarly the functions $f_{s\Omega}$ and $f_{t\Omega}$ account for finite-Reynolds-number deviations in the shear–rotation and translation–rotation couplings. In the limit of zero Reynolds number, these correction functions reduce to unity, i.e. $f_{st}(Re_s \to 0) \to 1$, $f_{s\Omega}(Re_s \to 0) \to 1$ and $f_{t\Omega}(Re_t \to 0) \to 1$. In the above equation, the additional subscript '0' in the lift coefficients correspond to the $Re \to 0$ limit. By comparing the first three terms of (3.10) and (3.11), we obtain

$$C_{Ls,w0} = \frac{2\lambda_1}{\pi}, \quad C_{Lt,w0} = \frac{2\lambda_2}{\pi} \quad \text{and} \quad C_{L\Omega,w0} = \frac{2\lambda_3}{\pi}. \tag{3.12}$$

Here we will consider scenarios where only two of these mechanisms are simultaneously active. Detailed simulations of shear–translation, shear–rotation and translation–rotation scenarios will be considered below. In this manner we will obtain best approximations to functions f_{st}, $f_{s\Omega}$ and $f_{t\Omega}$ that are valid over a range of Reynolds number. First, we will consider the case of a particle perfectly sliding on the wall, in which case the rotational motion of the particle is absent ($\Omega = 0$). The lift superposition given in (3.11) with the use of (3.12) can then be expressed as

$$C_{Lst,w}\left(Re_s, \frac{V_p}{G}\right) = \frac{C_{L,w}|_{\Omega=0}}{G^2} = C_{Ls,w} + C_{Lt,w}\left(\frac{V_p}{G}\right)^2 + \frac{\pi\lambda_4 C_{Ls,w}C_{Lt,w}}{2\lambda_1\lambda_2}\frac{V_p}{G}f_{st}\left(Re_s, \frac{V_p}{G}\right). \tag{3.13}$$

Second, we will consider the case of a particle undergoing rotation with the axis of rotation perpendicular to a linear shear flow, while the particle is in contact with the wall. Again the lift superposition given in (3.11) with the use of (3.12) reduces to

$$C_{Ls\Omega,w}\left(Re_s,\frac{\Omega}{G}\right)=\frac{C_{L,w}|_{V_p=0}}{G^2}=C_{Ls,w}+C_{L\Omega,w}\left(\frac{\Omega}{G}\right)^2 \\ -\frac{\pi\lambda_5 C_{Ls,w}C_{L\Omega,w}}{2\lambda_1\lambda_3}\frac{\Omega}{G}f_{s\Omega}\left(Re_s,\frac{\Omega}{G}\right). \quad (3.14)$$

In the above two relations, the division of $C_{L,w}$ by G^2 is tantamount to choosing $\tilde{G}d/2$ to be the velocity scale in the definition of the lift coefficients $C_{Lst,w}$ and $C_{Ls\Omega,w}$. From definition, we have $|V_p/G|=Re_t/Re_s$ and $|\Omega/G|=Re_\Omega/(2Re_s)$. Thus, $C_{Lst,w}$ and f_{st} can be re-expressed as functions of Re_s and Re_t, and similarly $C_{Ls\Omega,w}$ and $f_{s\Omega}$ can be re-expressed in terms of Re_s and Re_Ω. However, since we have followed the convention and defined the Reynolds numbers to be positive (see (2.3)), (3.13) has been defined to accommodate the relative directions of shear and translation and similarly (3.14) for shear and rotation.

Finally, we will consider the case of a particle undergoing both translation and rotation while in contact with the wall in an otherwise quiescent ambient fluid. The axis of rotation is parallel to the wall, but perpendicular to the direction of translation. Thus, depending on the magnitude of translation versus rotation, the particle can be considered to be sliding or rolling on the wall. The lift superposition given in (3.11) with the use of (3.12) reduces to

$$C_{Lt\Omega,w}\left(Re_t,\frac{\Omega}{V_p}\right)=\frac{C_{L,w}|_{G=0}}{V_p^2}=C_{Lt,w}+C_{L\Omega,w}\left(\frac{\Omega}{V_p}\right)^2 \\ -\frac{\pi\lambda_6 C_{Lt,w}C_{L\Omega,w}}{2\lambda_2\lambda_3}\frac{\Omega}{V_p}f_{t\Omega}\left(Re_t,\frac{\Omega}{V_p}\right). \quad (3.15)$$

Here the division of $C_{L,w}$ by $\tilde{V}_p^2$ translates to choosing $\tilde{V}_p$ to be the velocity scale.

3.2.2. *Drag superposition*

The drag superposition in the zero-Reynolds-number limit is simpler than that of the lift force. The drag force is given by a simple superposition of the shear, translation and rotation contributions and there are no cross-coupling contributions in the limit $Re \to 0$. At finite Re, nonlinear interaction will introduce cross-coupling between the different mechanisms. Following lift superposition, we define the overall superposition that is appropriate when all three mechanisms of shear, translation and rotation are simultaneously active to be expressed as a combination of the three individual mechanisms and their binary interactions. The composite drag superposition can then be expressed as

$$C_{D,\tilde{w}}=\frac{\tilde{F}_x}{\frac{\pi}{8}\rho d^2\tilde{V}^2}=C_{Ds,w}G|G|-C_{Dt,\tilde{w}}V_p|V_p|-C_{D\Omega,\tilde{w}}\Omega|\Omega| \\ -|G|V_p g_{st}\left(Re_s,\frac{V_p}{G}\right)-|G|\Omega g_{s\Omega}\left(Re_s,\frac{\Omega}{G}\right)-|V_p|\Omega\, g_{t\Omega}\left(Re_t,\frac{\Omega}{V_p}\right). \quad (3.16)$$

For simplicity, it is assumed that even when all three mechanisms are active, their nonlinear interaction can be described in terms of binary cross-couplings. It is thus assumed that simultaneous three-way interaction between shear, translation and rotation, and its effect on drag and lift forces are not important. The three correction functions, g_{st}, $g_{s\Omega}$ and $g_{t\Omega}$, embody the nonlinear binary cross-coupling between the different mechanisms. These corrections should vanish in the limit of zero Reynolds number, i.e. $g_{st}(Re_s \to 0) \to 0$, $g_{s\Omega}(Re_s \to 0) \to 0$ and $g_{t\Omega}(Re_t \to 0) \to 0$.

In the following sections we will consider the three cases of shear–translation, shear–rotation and translation–rotation binary superpositions one at a time and obtain the correction functions. In the case where a particle perfectly slides on the wall in a linear shear flow with the rotational motion of the particle being absent ($\Omega = 0$), the drag superposition reduces to

$$C_{Dst,\tilde{w}}\left(Re_s, \frac{V_p}{G}\right) = \frac{C_{D,\tilde{w}}|_{\Omega=0}}{G\,|G|} = C_{Ds,w} - C_{Dt,\tilde{w}}\frac{V_p}{G}\left|\frac{V_p}{G}\right| - \frac{V_p}{G} g_{st}\left(Re_s, \frac{V_p}{G}\right), \quad (3.17)$$

where g_{st} is the shear–translation drag correction to be determined. Next, when we consider the problem of particle undergoing pure rotation in a linear shear flow, while the particle is in contact with the wall, the following superposition of drag coefficient is proposed:

$$C_{Ds\Omega,\tilde{w}}\left(Re_s, \frac{\Omega}{G}\right) = \frac{C_{D,\tilde{w}}|_{V_p=0}}{G\,|G|} = C_{Ds,w} - C_{D\Omega,\tilde{w}}\frac{\Omega}{G}\left|\frac{\Omega}{G}\right| - \frac{\Omega}{G} g_{s\Omega}\left(Re_s, \frac{\Omega}{G}\right). \quad (3.18)$$

We then consider the case of a particle undergoing both translation and rotation while in contact with the wall in an otherwise quiescent ambient fluid. In this case, we propose the following superposition of drag coefficient:

$$C_{Dt\Omega,\tilde{w}}\left(Re_t, \frac{\Omega}{V_p}\right) = \frac{C_{D,\tilde{w}}|_{G=0}}{V_p\,|V_p|} = -C_{Dt,\tilde{w}} - C_{D\Omega,\tilde{w}}\frac{\Omega}{V_p}\left|\frac{\Omega}{V_p}\right| - \frac{\Omega}{V_p} g_{t\Omega}\left(Re_t, \frac{\Omega}{V_p}\right). \quad (3.19)$$

3.3. *Particle sliding on a wall in a linear shear flow*

Here we perform simulations of a particle in contact with a flat wall and sliding in the direction parallel to the shear flow. If the direction of sliding is against that of the shear flow, then drag and lift contributions tend to reinforce each other and become large. But, more likely the particle will slide in the direction of shear flow, and in this case, the relative velocity as seen by the particle decreases and the contributions to force from shear and translation tend to oppose each other.

Simulations were performed for a range of shear Reynolds number ($1 \leqslant Re_s \leqslant 100$) and a range of relative translation velocity ($-1 \leqslant V_p/G = 2\tilde{V}_p/(\tilde{G}d) \leqslant 0.75$). For $V_p/G = -1$, the particle velocity is the same as the local ambient shear flow velocity at $\tilde{y} = 0$ and since particle translates against the shear flow, the Reynolds number based on relative velocity becomes $2Re_s$. On the other hand, in the case of particle translating in the direction of shear flow, the simulations have considered only up to a translation velocity of 75 % of the local shear flow velocity at the centre of the particle. Figure 12(*a*) shows the computed lift coefficient plotted as symbols against Re_s for different values of V_p/G. In this figure the lift coefficient has been normalized with the shear velocity ($\tilde{G}d/2$) as the velocity scale and, in this non-dimensionalization, $C_{Lst,w}$ progressively decreases with increasing V_p/G. Instead, if the non-dimensionalization is with the relative velocity as the velocity scale, then the lift coefficient shown in figures must be scaled by $1/(1-(V_p/G))^2$. Note that the scaling factor is 0.25 for $V_p/G = -1$, but becomes 16 for $V_p/G = 0.75$. Thus, the lift coefficient increases with increasing V_p/G when non-dimensionalized by the relative velocity, which is consistent with the fact that the Reynolds number based on relative velocity decreases with increasing V_p/G (provided $V_p/G < 1$).

In order to evaluate the importance of the shear–translation coupling term, in figure 12(*b*) the computed lift coefficient minus $(C_{Ls,w} + C_{Lt,w}(V_p/G)^2)$ is plotted as

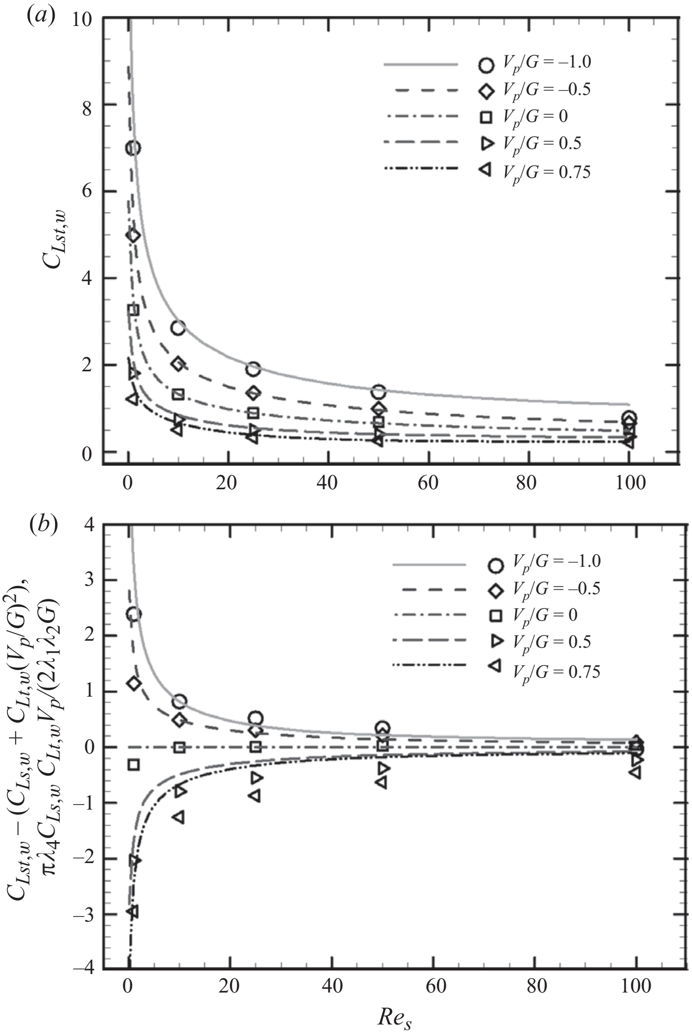

FIGURE 12. Lift coefficients of a translating particle in a linear shear flow. (*a*) Numerical results are presented as symbols and the superposition given in (3.14) is plotted as the lines. (*b*) Comparison of $(C_{Lst,w} - C_{Ls,w} - C_{Lt,w}(V_p/G)^2)$ (symbols) with the coupling term $\pi\lambda_4 C_{Ls,w} C_{Lt,w} V_p/(2\lambda_1\lambda_2 G)$ (lines).

symbols for the different combinations of Re_s and V_p/G considered. Also plotted in the figure as lines are the corresponding coupling terms $\pi\lambda_4 C_{Ls,w} C_{Lt,w} V_p/(2\lambda_1\lambda_2 G)$ evaluated using the curve fits given in (3.9). The ratio between the two corresponds to the shear–translation correction function, $f_{st}(Re_s, V_p/G)$. It can be readily seen that for $V_p/G \leqslant 0$, there is reasonable agreement between the symbols and the lines. Thus, when the particle translates against the shear, the proposed model is adequate to capture the combined effect of shear and translation without a correction factor. In contrast, the difference increases with V_p/G when the particle translates in the direction of shear flow reducing the relative velocity. Appendix A shows a simple empirical expression for $f_{st}(Re_s, V_p/G)$ obtained from the data presented in figure 12(*b*). The lift coefficients evaluated with the inclusion of the correction factor f_{st} (as given in (A 2)) are plotted in figure 12(*a*) as lines. The agreement is quite good.

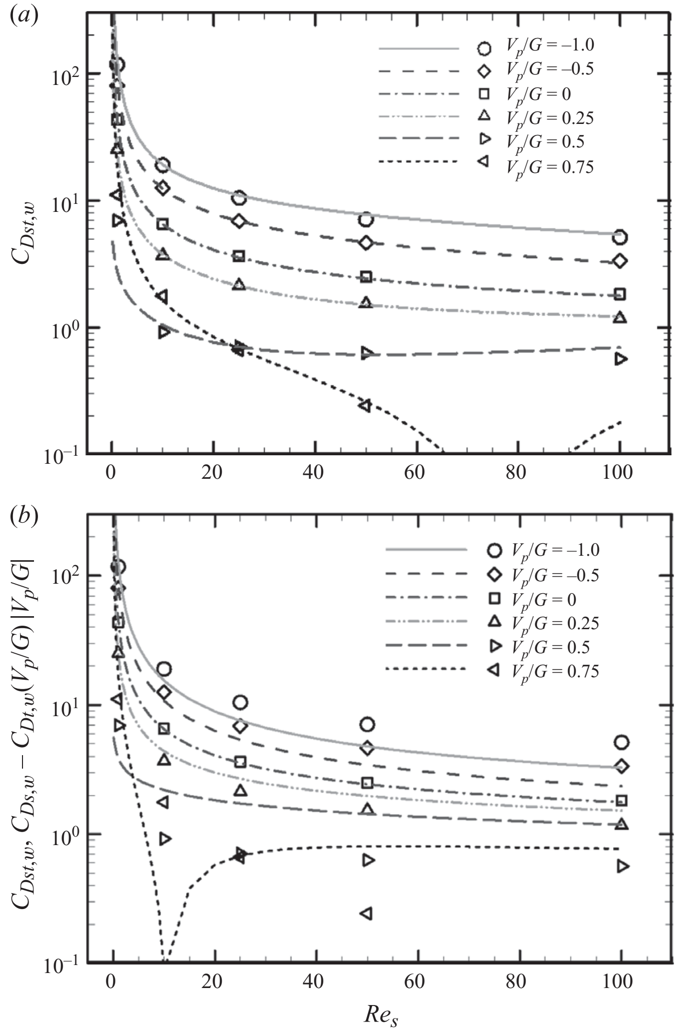

FIGURE 13. Drag coefficients of a sliding particle in a linear shear flow. (*a*) Numerical results are plotted as symbols and the proposed drag correlation (3.18) including the correction $g_{st}(Re_s, V_p/G)$ is shown as lines. (*b*) Comparison of simulation results (symbols) against the linear superposition of contributions, $C_{Ds,w} - C_{Dt,w}\left(V_p/G\right)|V_p/G|$ (lines). The difference between the two will be accounted for by the correction. For the case of $V_p/G = 0.75$, the drag coefficient is negative, so absolute values are shown.

The simulation results for the drag coefficient for the different cases are presented as symbols in figure 13(*a*). The drag coefficient decreases rapidly with increasing V_p/G and a log scale is used to capture this large variation. From (3.8) it can be seen that for a particle almost in contact with the wall ($L = 0.505$), the effect of translation on drag force dominates over that due to shear at small Reynolds number. This is to be expected due to the logarithmic increase in translational drag as the wall is approached. In particular, it can be seen that at small Reynolds numbers, the translational drag equals the shear drag when $Re_t \approx Re_s/2$. This in turn translates to $(V_p/G) \approx 0.5$. As a result, for a particle translating in the direction of shear, it can be expected that as non-dimensional translational velocity increases above 0.5, the drag force will reverse sign and point in the direction opposite to the ambient shear. The present finite-Reynolds-number simulation results for $V_p/G = 0.5$ remain positive, but substantially smaller and closer to zero. The drag force for $V_p/G = 0.75$ is observed to be consistently negative at all Reynolds numbers, which is in agreement with the theoretical expectation. Because of the log scale, in figures 13(*a*) and 13(*b*), the absolute value of the drag coefficient is shown for $V_p/G = 0.75$.

The computed drag presented in figure 13(*b*) was compared with the linear superposition as given by $C_{Ds,w} - C_{Dt,\tilde{w}}(V_p/G)|V_p/G|$, which was evaluated using the curve fits given in (3.8). As observed for the lift coefficient, the agreement between the actual drag and the linear superposition was observed to be quite good for $V_p/G \leqslant 0$. Thus, a simple addition of the shear and translation drag contributions is sufficient when the particle translates against the shear flow. In contrast, when the particle translates in the direction of shear, although the drag coefficient is small, it deviates from the simple addition of the individual contributions. Appendix A shows an empirical expression for $g_{st}(Re_s, V_p/G)$ obtained by curve fitting the difference between the actual computed drag and simple additive superposition. Figure 13(*a*) shows the proposed superposition (3.17), including the correction function $g_{st}(Re_s, V_p/G)$ plotted as lines along with the actual computed drag data (symbols). The agreement between the correlation and the actual data is satisfactory.

The flow streamlines for two sample cases of (*a*) $Re_s = 10$, $V_p/G = -1$ and (*b*) $Re_s = 10$, $V_p/G = 1$ are shown in figures 14(*a*) and 14(*b*). The streamlines are plotted in a frame attached to the particle. Thus, for the case of $V_p/G = 1$ in figure 14(*b*), the relative ambient flow below the particle centre is directed right to left, while that above the particle centre is directed left to right. This contributed to the large recirculation regions that exist both to the left and the right of the particle. For a particle translating against the shear flow ($V_p/G = -1$), in the frame attached to the particle, the ambient flow (including the wall) moves from left to right and the effect of the wake appears as a small region of reverse flow. The corresponding pressure contours for the above two cases are shown in figures 14(*c*) and 14(*d*). For the case of $V_p/G = -1$, the large fore–aft asymmetry contributes to the enhanced drag and the dominant low pressure above the particle is responsible for the enhanced lift force. In contrast, for $V_p/G = 1$, since the flow close to the wall has reversed direction in the frame moving with the particle, the high-pressure region is to the right lower side of the particle and, to the left lower side, the pressure is lower. This strong pressure difference over the lower half of the particle is due to the flow being forced to go around the small gap and is not compensated by the left-to-right ambient flow over the top part of the particle. This contributes to the drag reversal that was observed in figure 13. The pressure distribution is such that the contribution to lift is small. This behaviour qualitatively remains the same at higher Reynolds numbers as well.

The vortical structures, as extracted by iso-surface of swirling strength, for two cases $Re_s = 10$, $V_p/G = -1$ and $Re_s = 100$, $V_p/G = -1$ are shown in figures 14(*e*) and 14(*f*). When the particle translates counter to the shear flow, the relative velocity increases and the vortex structure intensifies. In particular, in figure 14(*f*), the Reynolds number based on relative velocity is 200 and a tendency towards downstream rollup of vortex structure can be seen (the flow still remains steady and there is no periodic shedding). When the particle translates in the direction of ambient shear, the vortex structures are observed to be relatively weak and are confined close to the particle.

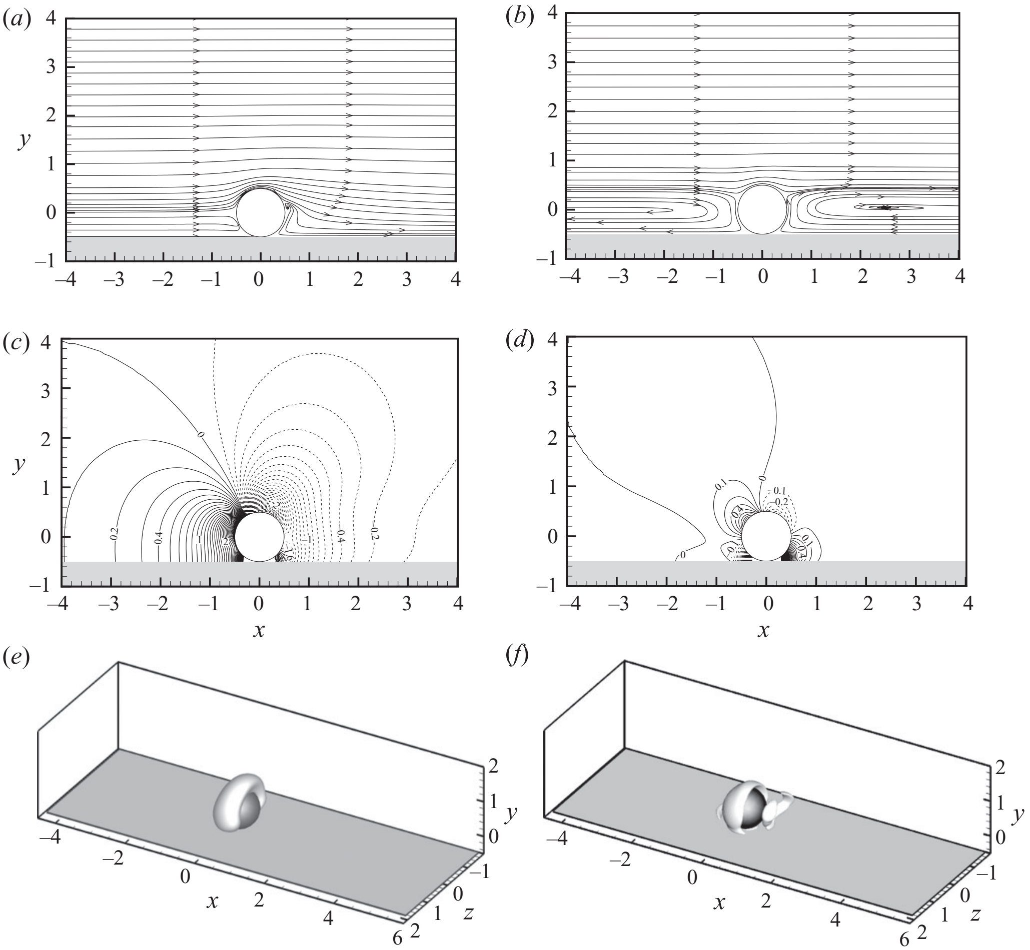

FIGURE 14. Flow features (streamlines, pressure contours and vortical structures ($\lambda_{ci} = 1.5$)) of a sliding particle in a linear shear flow. (*a*), (*c*) and (*e*) $Re_s = 10$, $V_p/G = -1$; (*b*) and (*d*) $Re_s = 10$, $V_p/G = 1$; (*f*) $Re_s = 100$, $V_p/G = -1$.

3.4. *Spinning particle very close to a wall in a linear shear flow*

Here we perform simulations of a particle close to a flat wall ($L = 0.505$) and spinning in the linear shear flow. The particle is fixed at a specified location and only allowed to spin along z-axis. If the direction of rotation is positive (counterclockwise as viewed in figure 1) and the shear flow is directed in the x-direction, then the drag contribution due to rotation tends to oppose that from shear, resulting in lower values of the drag force. On the other hand, more likely the x-directed shear flow will result in negative particle rotation (clockwise as seen in figure 1). In this case, particle rotation and ambient shear will cooperate to increase the drag force. Interestingly, as we will see below, the lift superposition behaves in a similar manner.

Simulations were performed for a range of shear Reynolds number ($1 \leqslant Re_s \leqslant 100$) and a range of relative rotation ($-1 \leqslant \Omega/G = \tilde{\Omega}/\tilde{G} \leqslant 1$). The relative velocity between the particle and the undisturbed ambient flow at the particle centre is the same as the shear velocity, since a rotating particle does not have any translational velocity. Figure 15(*a*) shows the lift coefficient against shear Reynolds number for different

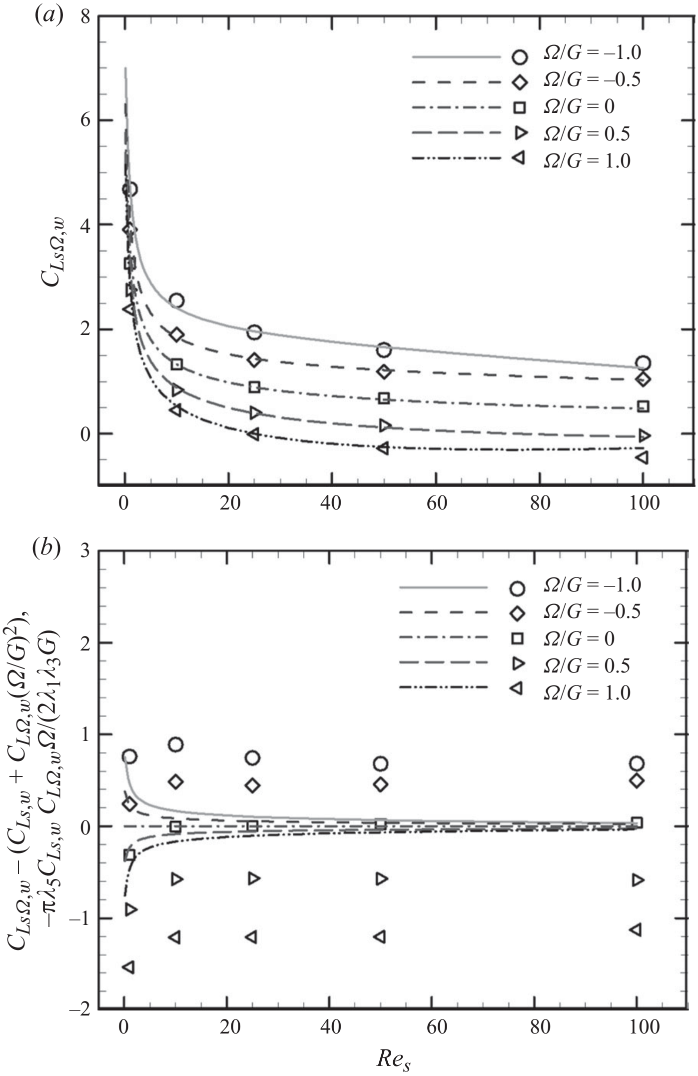

FIGURE 15. (*a*) Lift coefficients of a rotating particle in a linear shear flow; numerical results are presented as symbols and the superposition given in (3.15) is plotted as lines. (*b*) Comparison of $\left(C_{Ls\Omega,w} - C_{Ls,w} - C_{L\Omega,w}(\Omega/G)^2\right)$ (symbols) with the coupling term, $-\pi\lambda_5 C_{Ls,w} C_{L\Omega,w}\Omega/(2\lambda_1\lambda_3 G)$ (lines).

relative rotations. In the figure, the results of the numerical simulations are shown as symbols. As discussed above, substantial increase in lift results in the case of negative (clockwise) particle rotation and correspondingly a decrease in lift force can be observed in the case of positive (counterclockwise) particle rotation. The effect of rotation persists over the entire range of Reynolds number considered.

In order to evaluate the shear–rotation cross-coupling effect, the computed lift ($C_{Ls\Omega,w}$) minus ($C_{Ls,w} - C_{L\Omega,w}(\Omega/G)^2$) is plotted as symbols and the corresponding coupling term ($-\pi\lambda_5 C_{Ls,w} C_{L\Omega,w}\Omega/(2\lambda_1\lambda_3 G)$) as lines in figure 15(*b*). The difference between the two is considerable over the entire range of Reynolds number and rotation speeds, i.e. the shear–rotation coupling has a significant effect on lift. The

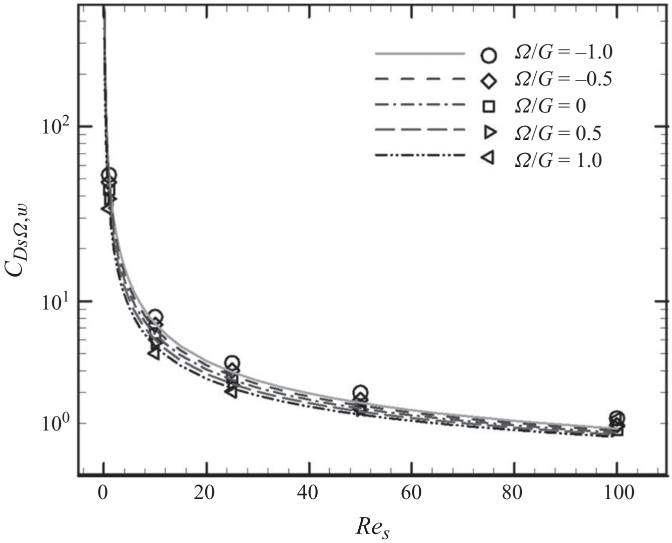

FIGURE 16. Drag coefficients of a rotating particle in a linear shear flow. Numerical results are plotted as symbols and the proposed drag correlation (3.19) including the correction $g_{s\Omega}(Re_s, \Omega/G)$ is shown as lines.

ratio between the two terms corresponds to the shear–rotation correction function, $f_{s\Omega}(Re_s, \Omega/G)$. In Appendix A, the computational results presented in figure 15(*b*) is used to develop an empirical correlation for $f_{s\Omega}(Re_s, \Omega/G)$. The lift correlation given in (3.14), with the expression (A 4) for $f_{s\Omega}$ taken into account, are plotted in figure 15(*a*) as lines. The agreement between the actual numerical result and the proposed correlation is good over the entire range.

In Figure 16 the drag coefficients evaluated from the numerical simulations are plotted as symbols for the various cases. It can be seen that the effect of particle rotation on drag is not very strong. Here we only consider linear superposition as given by $C_{Ds,w} - C_{D\Omega,\tilde{w}}(\Omega/G)|\Omega/G|$ and ignore the binary coupling term included in (3.18). The linear superposition is plotted as lines in figure 16. It is clear that linear superposition without considering the coupling terms $g_{s\Omega}(Re_s, \Omega/G)$ is sufficient to predict the drag coefficients under the conditions we considered here. Therefore, we conclude that in (3.16) and (3.18), we can assume $g_{s\Omega}(Re_s, \Omega/G) \approx 0$.

3.5. *Particle spinning and translating on a wall*

In this case, we perform simulations of a particle close to a flat wall ($L = 0.505$) and having both translation and rotation in a quiescent ambient fluid. The particle is considered to translate with velocity ($\tilde{V}_p$) parallel to the wall and rotate with an angular velocity ($\tilde{\Omega}$) about the z-axis. If a particle translates but does not rotate ($\tilde{\Omega} = 0$), then the particle can be considered to be in a pure 'sliding' motion. In the limit $\tilde{\Omega}d/(2\tilde{V}_p) = \Omega/V_p = -1$, the particle perfectly rolls on the wall without any slip. For other non-zero values of V_p and Ω, the particle is in a partial rolling and partial slipping state. The most likely scenario of rolling motion is one where $\tilde{V}_p$ and $\tilde{\Omega}$ are of opposite signs (i.e. $\tilde{V}_p\tilde{\Omega} < 0$). But, in the case of $\tilde{V}_p\tilde{\Omega} > 0$, a particle is translating with a back-spin or a reversed rotation. The problem of a sphere moving down an incline in a stagnant fluid has been considered in the past and theoretical and computational results (Cherukat & McLaughlin 1990; Zeng *et al.* 2005) suggest that the particle rotation under steady state (zero net drag and zero net torque) will

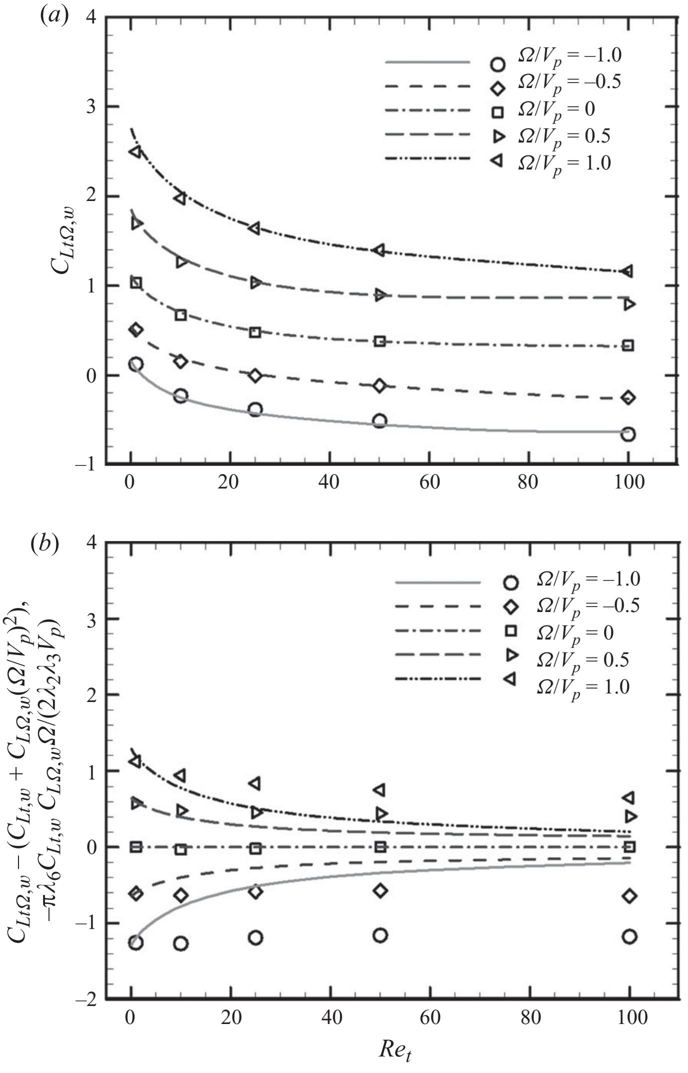

FIGURE 17. (*a*) Lift coefficients of a translating–rotating particle in a stagnant ambient flow; numerical results are presented as symbols and the superposition given in (3.16) is plotted as lines. (*b*) Comparison of $(C_{Lt\Omega,w} - C_{Lt,w} - C_{L\Omega,w}(\Omega/V_p)^2)$ (symbols) with the coupling term, $-\pi\lambda_6 C_{Lt,w} C_{L\Omega,w}\Omega/(2\lambda_2\lambda_3 V_p)$ (lines).

be such that particle rolls down the incline and that the rotation magnitude is weak. However, under conditions of non-Newtonian fluid or in the presence of multiple bounding walls, it has been observed experimentally that a particle can have reversed rotation (Humphrey & Murata 1992; Liu *et al.* 1993).

The computations were performed for a range of translation Reynolds number ($1 \leqslant Re_t \leqslant 100$) and a range of scaled rotational velocity ($-1 \leqslant \Omega/V_p \leqslant 1$). Of particular relevance to this case of translating–rotating particle is the recent experimental and numerical efforts of Stewart *et al.* (2010). They studied the structure and dynamics of the wake behind a translating particle under both forward and reverse rotations. Their investigation covers a translation Reynolds number ranging from 100 to 350 and thus covered both steady and unsteady wake regimes. Here, by restricting to only Reynolds number below 100, we consider only the steady wake regime. In figure 17(*a*) the

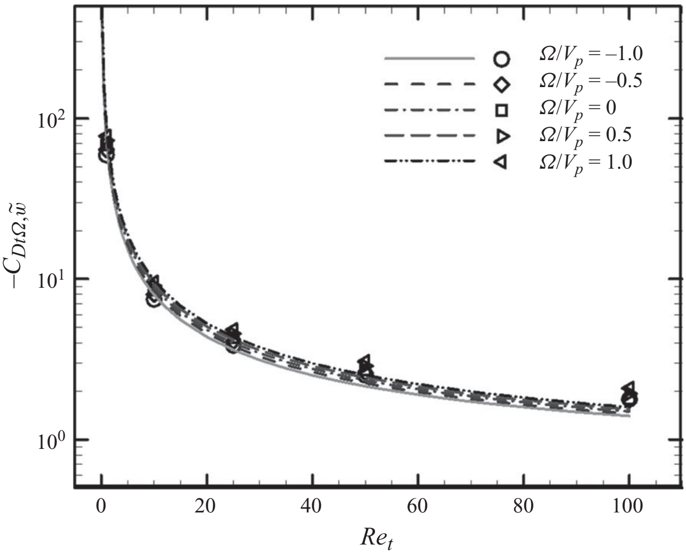

FIGURE 18. Drag coefficients of a translating–rotating sphere in a stagnant ambient flow. Numerical results are plotted as symbols and the proposed drag correlation (3.20) including the correction $g_{t\Omega}(Re_t, \Omega/V_s)$ is shown as lines.

numerically computed lift coefficient $C_{Lt\Omega,w}$ is plotted as symbols against Re_t for varying values of Ω/V_p. It can be seen that the lift coefficient monotonically decreases with increasing Re_t for all values of particle rotation considered. The lift coefficient for the cases of a positive Ω/V_p is larger and that for negative Ω/V_p is lower. In other words, a particle rotating with a back-spin will experience higher lift, while a particle rolling on the wall (rotational motion consistent with translation) will experience lower lift force. From the figure, it is clear that the effect of particle rotation on lift is significant.

In order to evaluate the role of the translation–rotation coupling term given in (3.15), in figure 17(*b*) the computed lift coefficient minus $C_{Lt,w} + C_{L\Omega,w}(\Omega/V_p)^2$ is plotted as symbols for different combination of Re_t and Ω. Also plotted in the figure as lines are the corresponding coupling term $-\pi\lambda_6 C_{Lt,w} C_{L\Omega,w}\Omega/(2\lambda_2\lambda_3 V_p)$ evaluated using the curve fits given in (3.9). The ratio between the two corresponds to the translation–rotation correction function, $f_{t\Omega}(Re_t, \Omega/V_p)$. In Appendix A we present the empirical expression for $f_{t\Omega}(Re_t, \Omega/V_p)$ obtained from the results presented in figure 17(*b*). Equation (3.15) is used to estimate the lift coefficient including the correction function given in (A 5) and the result is presented in figure 17(*a*) as lines along with the numerical results. The agreement between the two indicates the adequacy of the proposed correlation.

Figure 18 shows the drag coefficient plotted against the translational Reynolds number for different values of Ω/V_p. The drag coefficients obtained from the numerical simulations are shown as symbols. As in the case of shear–rotation coupling seen in figure 16, the effect of negative (clockwise) particle rotation is to decrease the drag, while the effect of positive rotation is to increase the drag, but the effect of particle rotation on the drag force is quite weak. The lines in figure 18 represent the linear superposition ($-C_{Dt,\tilde{w}} - C_{D\Omega,\tilde{w}}(\Omega/V_p)\,|\Omega/V_p|$) given in (3.19) without including the correction function $g_{t\Omega}$. From this figure, we can see that the effect of translation on drag is dominant and that of rotation is weak and can be ignored. We conclude

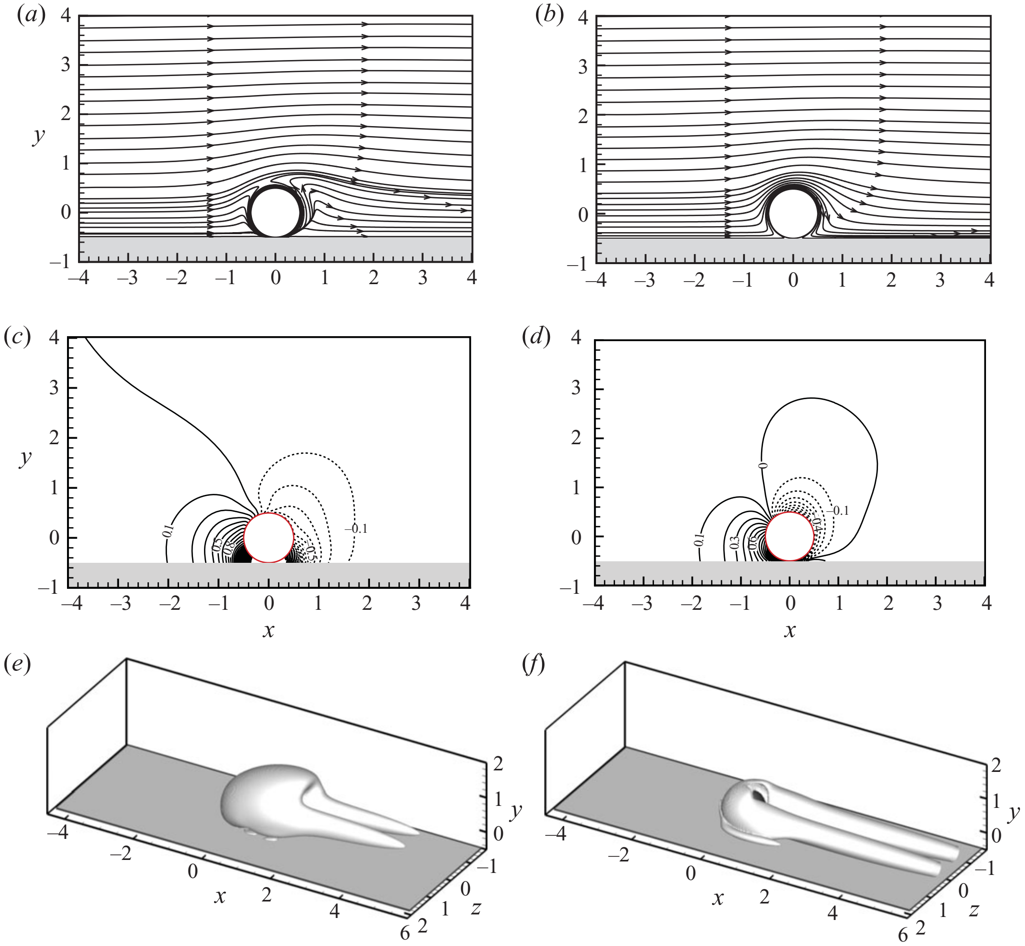

FIGURE 19. Flow features (streamlines, pressure contours and vortical structures ($\lambda_{ci} = 0.1$)) for a translating–rotating particle in a stagnant ambient fluid. (*a*), (*c*) and (*e*) $Re_t = 10,\ \Omega/V_p = -1$; (*b*), (*d*) and (*f*) $Re_t = 10,\ \Omega/V_p = 1$.

that the translation–rotation cross-term for drag could be ignored over the parameter range considered. Note that we show the negative of the drag coefficient ($-C_{Dt\Omega,\tilde{w}}$) in figure 18, since the dominant translation-induced drag ($C_{Dt,\tilde{w}}$) is defined to be positive in (3.8). The effect of the direction of translation on drag is accounted for through the denominator ($V_p\,|V_p|$) in (3.19). Also, the results are in good agreement with those of Stewart *et al.* (2010) obtained from their higher order accurate spectral element methodology. Their results nearly overlap on the present drag results and therefore are not explicitly shown in the figure.

The flow features are shown in figure 19 for two sample cases: (*a*, *c* and *e*) $Re_t = 10,\ \Omega/V_p = -1$ and (*b*, *d* and *f*) $Re_t = 10,\ \Omega/V_p = 1$. The streamlines for the two cases are shown in figures 19(*a*) and 19(*b*). Here we consider the particle to translate from right to left, i.e. $\tilde{V}_p < 0$. Since the streamlines are plotted in a frame attached to the particle, main flow is directed left to right. If the particle's translation and rotation are of opposite signs, i.e. $\Omega/V_p < 0$, then the particle's rotation is consistently rolling and for $\Omega/V_p = -1$, the particle is in perfect rolling motion. In this case, the bottom point of the particle that is in contact with the wall is stationary, while the relative velocity at the top of the particle is twice the translation velocity. The shear around the top surface of the particle is enhanced and, as can observed in figure 19(*a*), the flow behind a particle is dragged from the bottom to the top. In contrast, for $\Omega/V_p > 0$, the particle is in back-spin motion and thus the surface motion of the particle is the same as that of the ambient flow due to translation. In figure 19(*b*) ($\Omega/V_p = 1$), it can be seen that the flow smoothly passes along the particle surface without separation.

The corresponding pressure contours for the above two cases are shown in figures 19(*c*) and 19(*d*). The line contours are plotted in the range of −5 to 5 with 0.1 increments. As the particle is translating from right to left, the dominant high and low pressures are generated to the left and right of the particle. For $\Omega/V_p = -1$ in figure 19(*c*), since the particle rotates in counterclockwise direction, relatively higher and lower magnitude pressures are positioned at the small gap between the particle and the wall. In contrast, in figure 19(*d*), for $\Omega/V_p = 1$, we can see that lower pressure region is raised somewhat higher behind the particle since the back-spin of the particle contributes to accelerating the flow behind the particle. The corresponding pressure contours for both forward and reverse rotating particle at the higher translation Reynolds number of 100 are in good agreement with those presented in Stewart *et al.* (2010) and, as a result, they are not shown here. As seen earlier, this change in pressure distribution contributes to increase in both the drag and lift forces on the particle. Vortex formations of a translating and rotating particle are shown in figures 19(*e*) and 19(*f*) at the higher Reynolds number of 100. For $\Omega/V_p < 0$, since the shear above the particle increases, the vortex structure around the particle in its immediate surroundings in the wake region intensifies. At this higher *Re*, indications of a double threaded wake can be observed, which is often observed at higher *Re* even in the absence of particle rotation. For $\Omega/V_p = -1$, the particle rotation reduces shear above and in the wake of the particle, and thus, the vortex structure is absent on the symmetry plane, except at the front. A necklace-type vortex structure that is confined to the sides of the sphere is observed. The rotation of the streamwise vortex pair in this case is such that the fluid is pumped up away from the wall in the gap between the particle and the wall. Correspondingly, the induced motion is such that the lateral separation between the two legs remains nearly fixed as they extend downstream. These observations are exactly the same as those reported by Stewart *et al.* (2010) from both their experimental and computational results. The vortex structure at lower Reynolds numbers is much weaker and is confined to be around the sphere.

4. Conclusions

Here we have taken a step forward towards better understanding and modelling of hydrodynamic forces acting on a finite-sized particle moving near a plane wall in a linear shear flow. The drag and lift forces and torque on such a particle can be considered to arise from the superposition of three different mechanisms: forces due to shear, forces due to particle translation and forces due to particle rotation. In the limit of small Reynolds numbers, the drag on the particle can be simply given by a linear superposition of the three different mechanisms. In this limit, the lift force, however, has been shown to be a superposition of six contributions: three arise from the individual mechanisms (ambient shear, translation and rotation) while the other three contributions arise from shear–translation, translation–rotation and shear–rotation binary couplings (Krishnan & Leighton 1995).

Apart from the non-dimensional distance from the wall, three Reynolds numbers, namely shear, translation and rotation Reynolds numbers, can be defined and these four parameters together control the behaviour. The present investigation is limited to the case of a particle in contact with the wall. (In the case of particle translation and rotation, there is logarithmic singularity, and thus, in these cases, we consider a very small gap of 0.1 % between the particle and the wall.) The objective of the present paper is to extend the low-Reynolds-number understanding to finite Reynolds numbers and, in particular, we cover the range where the Reynolds numbers associated with each of the shear, translation and rotation mechanisms are limited to the range $0 \leqslant Re_s, Re_t, Re_\Omega \leqslant 100$. Note that the corresponding Reynolds number based on relative velocity has a larger range and in the case of particle translating against the shear flow, the Reynolds number based on relative velocity reaches 200.

Over this limited range of Reynolds number, the flow around the particle in all configurations considered here remains steady. For the case of a particle in an unbounded uniform ambient flow, the critical Reynolds number for the onset of unsteadiness has been shown to be about 270 (Johnson & Patel 1999; Bagchi, Ha & Balachandar 2001). The asymmetric effects of linear shear and the presence of a nearby wall are to decrease the critical Reynolds number, while the added viscous effect due to the wall will tend to delay the onset of unsteadiness to higher Reynolds number. Based on the results of Zeng *et al.* (2005) and Stewart *et al.* (2010) for a particle nearly in contact with a wall, the critical Reynolds number for unsteadiness can be expected to be higher than 300. Thus, all the results presented in this paper pertain to only the steady-flow regime.

Motivated by the low-Reynolds-number drag and lift superpositions, here we propose functional relations for drag and lift forces in terms of the three Reynolds numbers (see (3.11) and (3.16)) that are valid at finite *Re*. These expressions are physically motivated and rely on superposition of the individual mechanisms and their cross-coupling effects. Thus, investigations of finite-Reynolds-number behaviour of the following three elementary problems: (i) a stationary particle in contact with a wall in a linear shear flow, (ii) a translating particle almost in contact with a wall surrounded by quiescent fluid and (iii) a translating particle almost in contact with a wall surrounded by quiescent fluid, form the foundation on which the superposition is built. The former two problems (i and ii) and their finite-Reynolds-number expressions for drag and lift have already been addressed in Zeng *et al.* (2005, 2009). Here we first investigate in detail the problem of particle spinning near a flat wall in a quiescent fluid. The rotation Reynolds number and distance from the wall are systematically varied to obtain appropriate expressions for drag and lift forces. The corresponding finite Reynolds number drag and lift forces for the three different mechanisms are given in (3.8) and (3.9).

The proposed finite-Reynolds-number expression for drag and lift we recognize increased importance of nonlinearity and deviations from the low-Reynolds-number behaviour. For simplicity, we still limit coupling between the different mechanisms to be only binary in nature (shear–translation, shear–rotation and translation–rotation) and departure from the low Reynolds number is accounted in terms of correction functions. Here we consider the three binary interaction problems one at a time, namely (i) linear shear flow + translating particle, (ii) linear shear flow + rotating particle and (iii) translating + rotating particle in a stagnant ambient flow. We perform fully resolved simulations using the immersed boundary technique over a range of shear, translation and rotation Reynolds numbers. The simulation results are used to obtain approximate expressions for the correction functions ((A 2)–(A 5)).

Quantity	$C_{D,\Omega}$	$C_{L,\Omega}$	$C_{M,\Omega}$	$C_{Lst,w}$	$C_{Dst,\tilde{w}}$	$C_{Ls\Omega,w}$	$C_{Ds\Omega,\tilde{w}}$	$C_{Lt\Omega,w}$	$C_{Dt\Omega,\tilde{w}}$
Equation	(3.4)	(3.5)	(A1)	(3.13)	(3.17)	(3.14)	(3.18)	(3.15)	(3.19)
R^2	0.9998	0.9792	0.9752	0.9746	0.9835	0.9850	0.9975	0.9975	0.9385

TABLE 3. Goodness values computed as defined in (4.1) for the nine different empirical correlations presented for drag, lift and moment coefficients.

In summary, (3.11) together with (3.9), (A 2), (A 4) and (A 5) offer a composite expression for lift on a particle undergoing arbitrary motion in contact with the wall in a linear shear flow. The range of validity of these empirical relations is limited to Reynolds numbers (based on individual shear, translation and rotation mechanisms) being less than 100. Similarly, (3.16) together with (3.8) and (A 3) offer a composite expression for drag on a particle undergoing arbitrary motion in near contact with the wall ($L = 0.505$) in a linear shear flow. Efforts were made to keep these correlations simple, but at the same time, provide an accurate approximation for the computed direct-numerical-simulation (DNS) results. The accuracy of the correlations is evaluated with the R^2 goodness test defined as

$$R^2 = 1 - \frac{\sum (\xi_{fit} - \xi_{DNS})^2}{\sum (\xi_{DNS} - \bar{\xi}_{DNS})^2}, \tag{4.1}$$

where ξ_{DNS} represents any of the drag or lift correction obtained from the simulation results being interpolated and ξ_{fit} is the corresponding quantity obtained from the empirical relation. Here the sum is over all data points used in obtaining the empirical relation (for example, in the case of f_{st}, the summation is over all combinations of Re_s and V_p/G for which the simulations have been performed). Also the overbar indicates an average over all the data points. Thus, the goodness factor provides a measure of how well the empirical relation approximates the computed data in comparison to the distribution of the data. Table 3 shows the goodness for the nine empirical relations for drag, lift and moment coefficients presented in this paper.

A value close to 1 will correspond to very good approximation, while values far different from 1 will indicate inaccuracies in the approximation. It is clear from table 3 that all the empirical fits are good to within about 6 %. It should be pointed out that the empirical relations are not perfect and part of the error could be due to our restriction to only quadratic interactions in the model. Further improvement could be made by extending the model to include higher order interactions. But such an attempt was not pursued, partly due to its complexity and partly due to the reasonable success in approximating only with the quadratic coupling.

We envision the above-presented correlations to be used in accurate computations of particle motion through wall-bounded shear flows. In this context, even if the wall-bounded flow is steady, the particle motion can be unsteady. For instance, the particle can be moving towards or away from the wall, or could be accelerating or decelerating along the streamwise direction. The present paper will only provide improved approximations for the quasi-steady component of drag and lift forces, based on local shear, and instantaneous translational and rotational motions of the particle. Depending on particle-to-fluid density ratio, additional unsteady forces might become important in dictating the particle motion. The presence of the wall can have an influence on the unsteady added mass and history forces and contribute to deviations from their classic behaviour. Such effects are not well understood and, if important, must be taken into account in order to accurately follow the unsteady dynamics of particles close to a solid boundary.

This work was partially supported by the Korean Research Foundation Grant funded by the Korean Government (KRF-2007-357-D00032). The authors acknowledge the University of Florida High-Performance Computing Centre for providing computational resources and support that have contributed to the research results reported within this paper.

Appendix. Empirical expression obtained from the numerical data

Moment coefficient of a particle rotating in quiescent fluid near a flat wall. The numerical results for the moment coefficient of a particle undergoing pure rotational motion close to a wall shown in figure 10 are used to obtain the following empirical expression:

$$C_{M,\Omega} = \exp(-3\varepsilon)\left[-\frac{64}{Re_\Omega}(1+0.0011Re_\Omega)\left(\frac{2}{5}\ln\varepsilon - 0.3817\right)\right] + (1-\exp(-4\varepsilon)) \times \left[\frac{64}{Re_\Omega}\left(1+\frac{5}{16(1+\varepsilon)^3}\right) + 0.00225Re_\Omega\right] \text{ for all } \varepsilon,\ Re_\Omega \leqslant 100. \qquad \text{(A 1)}$$

This expression reduces to the low-Reynolds-number theories as $Re \to 0$. The above expression is shown in figure 10(*a*) as lines and can be seen to well approximate the numerical results.

Lift contribution from shear–translation binary coupling. The data presented in figure 12(*b*) over a range of Re_s and V_p/G are used to develop a simple approximation for $f_{st}(Re_s, V_p/G)$, which is given below:

$$f_{st}\left(Re_s, \frac{V_p}{G}\right) = 1 + \left(2.156\left(\frac{V_p}{G}\right)^2 + 1.789\frac{V_p}{G} + 0.704\right)\tanh(0.02Re_s). \qquad \text{(A 2)}$$

In the small-shear-Reynolds-number limit ($Re_s \ll 1$), the above empirical expression approaches the correct limit of unity ($f_{st}(Re_s \to 0, V_p) \to 1$). Therefore, the lift correlation given in (3.14) correctly matches with Krishnan & Leighton's (1995) theory.

Drag contribution from shear–translation binary coupling. The difference between the actual computed drag and that obtained from an additive superposition of only the shear and translation is shown in figure 13(*b*). These data are used to obtain an approximate estimation of $g_{st}(Re_s, V_p/G)$ as given below:

$$g_{st}\left(Re_s, \frac{V_p}{G}\right) = \left(2.03\frac{V_p}{G} - 8.18\right)Re_s^{0.3} - \left(2.8\frac{V_p}{G} - 10.73\right)Re_s^{0.25}. \qquad \text{(A 3)}$$

The above expression reaches the correct limit of $g_{st}(Re_s \to 0, \frac{V_p}{G}) \to 0$.

Lift contribution from shear–rotation binary coupling. Using the results presented in figure 15(*b*) we have developed a simple approximation for $f_{s\Omega}(Re_s, \Omega/G)$, which is given below as

$$f_{s\Omega}\left(Re_s, \frac{\Omega}{G}\right) = 1 + \left(0.251\frac{\Omega}{G} + 1.018\right)Re_s^{0.66}. \qquad \text{(A 4)}$$

The above correction function has been developed to satisfy the requirement that in the small-shear-Reynolds-number limit ($Re_s \ll 1$), the correction function $f_{s\Omega}$ must approach a value of unity. Note that the lift correlation given in (3.14) thus matches with Krishnan & Leighton's (1995) theory in the low-Reynolds-number limit.

Lift contribution from translation–rotation binary coupling: The results presented in figure 17(*b*) are used to obtain the following correlation:

$$f_{t\Omega}\left(Re_t, \frac{\Omega}{V_p}\right) = 1 + \left[0.0122\frac{\Omega}{V_p}\left(\frac{\Omega}{V_p} - 2\right) + 0.0548\right] Re_t^{0.85}. \tag{A 5}$$

As in the other correction functions, in the zero-Reynolds-number limit ($Re_t \rightarrow 0$), the above function asymptotically approaches unity (i.e. $f_{t\Omega}(Re_t \rightarrow 0, \Omega/V_p) \rightarrow 1$) and thus the lift correlation matches with the Krishnan & Leighton's (1995) theory in the low-Reynolds-number limit.

REFERENCES

Bagchi, P., Ha, M. Y. & Balachandar, S. 2001 Direct numerical simulation of flow and heat transfer from a sphere in a uniform crossflow. *ASME J. Fluids Engng* **123**, 347–358.

Chakraborty, P., Balachandar, S. & Adrian, R. J. 2005 On the relationships between local vortex identification schemes. *J. Fluid Mech.* **535**, 189–214.

Cherukat, P. & McLaughlin, J. B. 1990 Wall-induced lift on a sphere. *Intl J. Multiphase Flow* **16**, 899–907.

Cherukat, P. & McLaughlin, J. B. 1994 The inertial lift on a rigid sphere in a linear shear flow field near a flat wall. *J. Fluid Mech.* **263**, 1–18; Corrigendum 1995 *J. Fluid Mech.* **285**, 407.

Goldman, A. J., Cox, R. G. & Brenner, H. 1967*a* Slow viscous motion of a sphere parallel to a plane wall – I Motion through a quiescent fluid. *Chem. Engng Sci.* **22**, 637–651.

Goldman, A. J., Cox, R. G. & Brenner, H. 1967*b* Slow viscous motion of a sphere parallel to a plane wall – II Couette flow. *Chem. Engng Sci.* **22**, 653–660.

Humphrey, J. A. C. & Murata, H. 1992 On the motion of solid spheres falling through viscous fluids in vertical & inclined tubes. *ASME J. Fluids Engng* **114**, 2–11.

Johnson, T. A. & Patel, V. C. 1999 Flow past a sphere up to a Reynolds number of 300. *J. Fluid Mech.* **378**, 19–70.

King, M. R. & Leighton, D. T. 1997 Measurement of the inertial lift on a moving sphere in contact with a plane wall in a shear flow. *Phys. Fluids* **9**, 1248–1255.

Krishnan, G. P. & Leighton, D. T. 1995 Inertial lift on a moving sphere in contact with a plane wall in a shear flow. *Phys. Fluids* **7**, 2538–2545.

Leighton, D. T. & Acrivos, A. 1985 The lift on a small sphere touching a plane in the presence of a simple shear flow. *Z. Angew. Math. Phys.* **36**, 174–178.

Liu, Y. J., Nelson, J., Feng, J. & Joseph, D. D. 1993 Anomalous rolling of spheres down an inclined plane. *J. Non-Newton. Fluid Mech.* **50**, 305–329.

Małysa, K. & van de Ven, T. G. M. 1986 Rotational and translational motion of a sphere parallel to a wall. *Intl J. Multiphase Flow* **12**, 459–468.

McLaughlin, J. B. 1993 The lift on a small sphere in wall-bounded linear shear flows. *J. Fluid Mech.* **246**, 249–265.

Roma, A., Peskin, C. & Berger, M. 1999 An adaptive version of the immersed boundary method. *J. Comput. Phys.* **153**, 509–534.

Saff, E. B. & Kuijlaars, A. B. J. 1997 Distributing many points on a sphere. *Math. Intelligencer* **19**, 5–11.

Saffman, P. G. 1965 The lift on a small sphere in a slow shear flow. *J. Fluid Mech.* **22**, 385–400; Corrigendum 1968 *J. Fluid Mech.* **31**, 624.

Schiller, L. & Naumann, A. 1933 Uber die grundlegenden berechnungen bei der schwerkraftaufbereitung. *Ver. Deut. Ing.* **77**, 318.

Stewart, B. E., Thompson, M. C., Leweke, T. & Hourigan, K. 2010 Numerical and experimental studies of the rolling sphere wake. *J. Fluid Mech.* **643**, 137–162.

TAKEMURA, F. & MAGNAUDET, J. 2003 The transverse force on clean and contaminated bubbles rising near a vertical wall at moderate Reynolds number. *J. Fluid Mech.* **495**, 235–253.

TAKEMURA, F., TAKAGI, S., MAGNAUDET, J. & MATSUMOTO, Y. 2002 Drag and lift forces on a bubble rising near a vertical wall in a viscous liquid. *J. Fluid Mech.* **461**, 277–300.

UHLMANN, M. 2005 An immersed boundary method with direct forcing for the simulation of particular flows. *J. Comput. Phys.* **209**, 448–476.

VASSEUR, P. & COX, R. G. 1976 The lateral migration of a spherical particle in two-dimensional shear flows. *J. Fluid Mech.* **78**, 385–413.

ZANG, Y., STREET, R. L. & KOSEFF, J. R. 1994 A non-staggered grid, fractional step method for time-dependent incompressible Navier–Stokes equations in curvilinear coordinate. *J. Comput. Phys.* **114**, 18–33.

ZENG, L. 2007 Interaction between a spherical particle and wall-bounded flows at finite Reynolds number. Ph.D thesis, University of Illinois at Urbana-Champaign, Urbana-Champaign, IL.

ZENG, L., BALACHANDAR, S. & FISHER, P. 2005 Wall-induced forces on a rigid sphere at finite Reynolds number. *J. Fluid Mech.* **536**, 1–25.

ZENG, L., BALACHANDAR, S., FISHER, P. & NAJJAR, F. 2008 Interactions of a stationary finite-sized particle with wall turbulence. *J. Fluid Mech.* **594**, 271–305.

ZENG, L., NAJJAR, F., BALACHANDAR, S. & FISHER, P. 2009 Forces on a finite-sized particle located close to a wall in a linear shear flow. *Phys. Fluids.* **21**, 033302.

ZHOU, J., ADRIAN, R. J., BALACHANDAR, S. & KENDALL, T. M. 1999 Mechanisms for generating coherent packets of hairpin vortices in channel flow. *J. Fluid Mech.* **387**, 353–396.